ELSEVIER

Contents lists available at ScienceDirect

Coastal Engineering

journal homepage: www.elsevier.com/locate/coastaleng



Investigating wave shape effect on sediment transport over migrating ripples using an eulerian two-phase model

Ali Salimi-Tarazouj ^{a,b,c,d,*}, Tian-Jian Hsu ^e, Peter Traykovski ^f, Julien Chauchat ^g

- ^a NWS/NCEP/Environmental Modeling Center, National Oceanic and Atmospheric Administration (NOAA), College Park MD, USA
- ^b Lynker, Leesburg, VA, 20176, USA
- ^c University of Maryland, College Park, MD, 20742, USA
- d Formerly at Center for Applied Coastal Research, Department of Civil and Environmental Engineering, University of Delaware, Newark, DE, USA
- ^e Center for Applied Coastal Research, Civil and Environmental Engineering, University of Delaware, Newark, DE, 19716, USA
- ^f Applied Ocean Physics and Engineering, Woods Hole Oceanographic Institution, Woods Hole, MA, 02543, USA
- ^g University of Grenoble Alpes, LEGI, F-38000, Grenoble, France

ARTICLE INFO

Keywords: Two-phase model SedFoam Sediment transport Sand ripples Wave shape effect

ABSTRACT

A Reynolds-averaged two-phase Eulerian model for sediment transport, SedFoam, is utilized in a twodimensional domain for a given sediment grain size, flow period, and mobility number to study the asymmetric and skewed flow effects on the sediment transport over coarse-sand migrating ripples. First, the model is validated with a full-scale water tunnel experiment of orbital ripple driven by acceleration skewed (asymmetric) oscillatory flow with good agreement in the flow velocity, net sediment transport, and ripple migration rate. The model results showed that the asymmetric flow causes a net onshore sediment transport of both suspended and near-bed load (the conventional bed load and part of the near-bed suspended load, responsible for ripple migration). The suspended load transport is driven by the "positive phase-lag" effect, while the near-bed transport is due to the large erosion of the boundary layer on the stoss flank, sediment avalanching on the lee flank, and the returning flux induced by the stoss vortex. Together, these processes result in a net onshore transport rate. In contrast, for an energetic velocity skewed (skewed) flow, the net transport rate is offshore directed. This is due to a larger offshore-directed suspended load transport rate, resulting from the "negative phase-lag" effect, compared to the onshore-directed near-bed load transport rate. Compared to the asymmetric flow, the onshore near-bed load transport (and migration) rate is limited by the larger offshore directed flux associated with returning flow on the lee side, due to a stronger lee vortex generation during the onshore flow half-cycle. In the combined asymmetric-skewed case, the near-bed load and migration rate are higher than in the asymmetric flow case. Moreover, the offshore-directed suspended load is much smaller compared to the skewed flow case due to a competition between the negative (due to velocity skewness) and positive (due to acceleration skewness) phase-lag effects. As a result, the net transport rate is onshore directed but slightly smaller than the asymmetric flow case.

1. Introduction

Sediment transport due to wave action in near-shore sandy beach regions can occur in various forms and magnitudes (e.g., sheet flows, migrating ripples) depending on wave energy intensity. Predicting the cross-shore net sediment transport rate, which is the subtle balance between the net near-bed load and suspended load transport rates, has been an important topic in the coastal engineering research (Hurther and Thorne, 2011; vander et al., 2013). The shape of wave orbital

velocity, quantified by velocity and acceleration skewness, is a key factor for predicting the cross-shore net sediment transport magnitude and direction in the shoaling and surf zones (Sherwood et al., 2022).

Sheet flows, occurring under strong wave action, involve sediment transport in the uppermost sediment layer where particle-particle interactions dominate. Research extensively covers the impact of skewed flow (resulting from sharp crests and broad troughs; blue solid line in Fig. 1) and asymmetric flow (associated with forward-leaning and near-breaking waves; black dash line in Fig. 1) on sheet flow sediment

^{*} Corresponding author. Lynker, Leesburg, VA, 20176, USA. E-mail address: ali.salimi@noaa.gov (A. Salimi-Tarazouj).

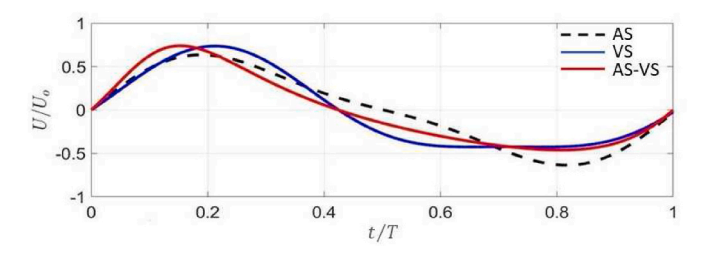


Fig. 1. The free stream velocity time-series for asymmetric (black dash-line), skewed (blue solid line), and asymmetric-skewed (combined) (red solid line) flows.

transport. Coarse sand ($D_50 = 0.4-1$ mm) in long-period waves (T =5-12 s) experiences positive skewed flow, driving onshore-directed net transport. Conversely, finer sediment (D_50 = 0.063-0.25 mm) or shorter waves (T = 2.5–5 s) exhibit reduced onshore transport due to the "phase-lag" effect. Asymmetric flow effects were initially proposed by King (1991) and have mainly been studied in sheet flows. Watanabe and Sato (2005) and others demonstrated that net transport aligns with the highest acceleration and increases with flow asymmetry, with Ruessink et al. (2011) identifying a phase-lag effect driving onshore transport in fine sand under asymmetric flows. Studies on the combined effects of asymmetric-skewed flows (red solid line in Fig. 1) in sheet flow conditions, which are common in the surf zone, are limited but suggest that a significant bed shear stress skewness can enhance onshore transport unless the phase-lag effect intervenes, particularly for fine sand or short-period flows (Dong et al., 2013; Ruessink et al., 2011; Dibajnia and Watanabe, 1998; Rafati et al., 2021).

Ripples can form under skewed and/or asymmetric flows during moderate wave energy conditions with ripple lengths (λ) and heights (η) ranging from 10 to 100 cm and 1–10 cm, respectively (Thornton et al., 1998; Wengrove et al., 2018). For sufficiently high ripple steepness (η/λ > 0.1), periodic vortex generation-ejection process occurs during each flow half-cycle (Hurther and Thorne, 2011; Longuet-Higgins, 1981), which can suspend a significant amount of sediment into the water column (van der Werf et al., 2007), and hence, even for the coarse sand ripples, the phase-lag effect is found to be an important transport mechanism. The existing understanding of the sediment transport mechanisms over migrating ripples is mainly based on laboratory studies driven by skewed flows (Hurther and Thorne, 2011; Ribberink et al., 2008; van der Werf et al., 2007). Large-scale oscillatory water-tunnel experiments (van der Werf et al., 2007; Ribberink et al., 2008) showed that the phase-lag effect causes a net offshore directed suspended load above ripples driven by skewed (Stokes 2nd order) oscillatory flows; large onshore flow velocities suspend more sediment over the lee (onshore) flank through a strong vortex generation-ejection process (compared to the sediment suspended over the stoss [offshore] flank), and via the phase-lag effect, these suspended sediments are transported offshore during the offshore half-cycle. Meanwhile, a net near-bed load transport forces onshore ripple migration which is directly associated with the onshore directed velocity skewness (Salimi-Tarazoui et al., 2021a; Traykovski et al., 1999; Wengrove et al., 2019). Hence, the net cross-shore transport rate above ripples driven by skewed flows is a subtle balance between the net offshore directed suspended load (dictated by the phase-lag effect) and the net onshore directed near-bed load. van der A et al. (2013) developed a novel empirical equation for calculating the net sand transport induced by non-breaking waves and currents. The equation is specifically designed for cross-shore sand transport in wave-dominated conditions and is based on the concept of semi-unsteady, half wave-cycle, using bed shear stress as the primary driving parameter. The formula also incorporates the effects of unsteady phase-lag between velocities and concentrations, which is particularly crucial for rippled bed and fine sand sheet-flow environments.

Investigation of the asymmetric flow effect on sediment transport

over sand ripples, including ripple geometry, flow field, and net sediment transport rate, is very recent (Wang and Yuan, 2019, 2020; Yuan and Wang, 2019). Yuan and Wang (2019) first showed that onshore (forward-leaning) asymmetric oscillatory flow changes the periodic vortex generation-ejection process over ripples, resulting in more residual turbulence being transferred toward the lee (onshore) flank during the onshore half-cycle. Wang and Yuan (2020) observed that both the ripple migration and net transport rate over ripples driven by onshore asymmetric flows are always onshore directed and increase with the flow asymmetry. For the suspended load over ripples, Wang and Yuan (2020) reported a net onshore directed suspended load contrary to the offshore directed net suspended load in skewed flows due to the phase-lag effect. Based only upon the measured velocity field, the fast offshore deceleration phase allows less time for the suspended sediment by the vortex generation-ejection over the stoss flank to settle down before traveling to the onshore side during the onshore half-cycle, while the opposite happens on the lee side. This leads to a net onshore-directed suspended load similar to the phase-lag effect in the sheet flows driven by onshore asymmetric flows (Ruessink et al., 2011).

Recent studies (e.g., Hurther and Thorne, 2011; Kranenburg et al., 2013; van der Werf et al., 2007) have highlighted significant differences in sediment transport between oscillatory water tunnel flows (horizontally uniform flows) and free surface waves, particularly for sheet flows and migrating ripples. Van der Werf et al. (2007) observed a small offshore boundary layer streaming in oscillatory water tunnel experiments, driven by flow acceleration and vortex generation over ripple crests. This streaming, although small compared to horizontal orbital velocity, is important due to its presence in the near-bed high concentration region. Hurther and Thorne (2011) reported a large onshore directed sediment flux below the ripple crests under the shoaling surface wave which is larger than the offshore directed suspended flux above the ripple crest due to larger lee vortex generation-ejection process. In the case of free surface waves, the region close to the bed influences the phase of horizontal and vertical orbital velocities, leading to a net downward transport of horizontal momentum over the wave cycle. This downward momentum transfer generates an onshore current within the boundary layer, known as "progressive wave streaming" (Longuet-Higgins, 1953). The progressive wave streaming can enhance the onshore net transport rate for medium and coarse sand (Dohmen-Janssen and Hanes, 2002) or even produce an onshore directed net transport rate for the fine sand sheet flows (Schretlen, 2012). In this study, our focus is specifically on the wave-shape effect on sediment transport over migrating ripples driven by oscillatory flows, and the presence of progressive wave streaming is not considered.

Due to the complex coupling between the morphology, sediment transport, and hydrodynamics, numerical models were mostly used to study the periodic vortex generation-ejection over fixed ripples (Blondeaux and Vittori, 1991; Chang and Hanes, 2004; Longuet-Higgins, 1981; Onder and Yuan, 2019; van der Werf et al., 2008; Zedler and Street, 2006). The main difference between these studies is the modeling of the turbulence field. Although these studies reveal the characteristics of the vorticity field above ripples, they ignore the interaction of the migrating and evolving ripple bed with the flow field. Hence, a few studies have utilized the standard suspended load/bedload formulations for sediment transport to simulate the ripple migration and evolution driven by oscillatory flows (Chou and Fringer, 2010; Marieu et al., 2008). This type of approach requires empirical formulas for different transport mechanisms (e.g., bedload transport rate, sediment avalanching, and reference concentration). On the other hand, the high fidelity two-phase LES-DEM model used by Finn et al. (2016) simulates the ripple migration under the skewed flow successfully. Although this type of Euler-Lagrange approach can accurately model the complex particle-particle interactions and particle-fluid interactions, the application to ripple migration study is limited due to a high computational

To model ripple evolution and migration while avoiding suspended

load/bedload assumptions, Salimi-Tarazouj et al. (2021a, b) solve the Reynolds-Averaged Eulerian two-phase equations for fluid and sediment phases using the open-source model, SedFoam (Chauchat et al., 2017; Cheng et al., 2017). Salimi-Tarazouj et al. (2021a) validated SedFoam for onshore migrating ripples driven by a skewed flow in an oscillating water tunnel experiment reported by van der Werf et al. (2007). Sed-Foam simulation results confirmed the offshore-directed net suspended load is due to the phase-lag effect, which is dictated by the vortex generation-ejection process. The model also showed an imbalance in the near-bed load (sediment transport rate within a few grains diameter above the ripple surface, see equation (5)) associated with more intense boundary layer flow speed-up during the onshore flow cycle and sediment avalanching near the lee ripple flank which forces the onshore ripple migration. Later, Salimi-Tarazouj et al. (2021b) utilized the SedFoam model to simulate ripple evolution due to several step-changes in the oscillatory flow forcing, including the transition to sheet flows and ripple reformation from a fairly flatbed, and confirmed the role of near-bed load and suspended load transport in the growing and diminishing of sand ripples.

Although previous research has explored the net sediment transport rate and flow field over migrating ripples under skewed and asymmetric flows, little is known about the impact of asymmetric flows on different near-bed load sediment transport mechanisms. Additionally, no detailed study has investigated sediment transport over migrating ripples driven by combined flows. In this study, Sedfoam is utilized to simulate sediment transport over migrating ripples driven by skewed, asymmetric, and combined oscillatory flows with the same root-mean-square flow intensity for a given flow period and sediment grain size. The model results for the asymmetric flow case are validated using the Yuan and Wang (2019) water tunnel experiment, while the results for the other two cases are compared against the asymmetric flow case to investigate the effect of wave shape on different sediment transport fluxes over the migrating ripples. Therefore, our study aims to elucidate the mechanisms through which suspended and near-bed load contribute to the net transport rate over ripples driven by oscillatory flows with different shapes. Section 2 describes the methodology, section 3 presents the model results, and section 4 offers a discussion, with concluding remarks provided in Section 5.

2. Methodology

The sediment transport model presented in this paper is based on the Eulerian-Eulerian two-phase formulation implemented in the open-source software SedFoam. The two-phase model equations for incompressible fluids and sediment are provided in Appendix A and are based on the previous publications (Chauchat et al., 2017; Cheng et al., 2017; Salimi-Tarazouj et al., 2021a, b). Salimi-Tarazouj et al. (2021a, b) extended the model application to simulate sand ripple dynamics in a 2D vertical model domain using Reynolds-averaged formulations with the $k\text{-}\epsilon$ turbulence closure model for both fluid and sediment phases. The

model equations allow for seamless integration of turbulence, particle-fluid, particle-particle interactions, and ripple bed dynamics into a single modeling framework and thus avoid artificial separation of transport into near-bed load and suspended load layers.

In line with Salimi-Tarazouj et al. (2021a, b), to create a stable ripple bed, we utilize a sediment concentration profile derived from a one-dimensional vertical simulation conducted after the flow has reached equilibrium (Cheng et al., 2017). This sediment concentration profile is mapped to every vertical (z-direction) grid column throughout the entire streamwise (x) direction in the model domain with the vertical location of each profile adjusted by the prescribed initial sinusoidal bathymetry (see Fig. 2). This mapping procedure is required to establish appropriate initial contact stresses $P^{sf} = f(\varphi)$ and $\tau^{sf} = f(P^{sf})$ (see Appendix A, equations A.7-A.9) in the ripple bed and prevent unrealistic initial slumping.

Fig. 2 shows a schematic plot of the model domain. At the top boundary, a free-slip (i.e., Neumann) boundary condition is used for both the fluid and sediment phase quantities. At the bottom of the model domain, a no-slip boundary condition is applied for the velocities of both phases while a zero-gradient boundary condition is specified for other quantities. It is reminded that in the present two-phase model, the whole profiles of primary variables throughout the water column down to the immobile bed are resolved, and the no-slip boundary at the bottom of the model domain plays a minor role in the results because it is under a sufficiently thick layer of immobile sediment bed. To minimize computational domain length, periodic boundary conditions are specified at the two lateral boundaries. The scheme used for the divergence operators of the different quantities is a blend between a pure centered second order scheme and a first order upwind scheme in the regions of rapidly changing gradient ("limitedLinear 1"). The laplacian scheme for all quantities is a linear interpolation with non-orthogonality correction ("Gauss linear corrected").

In this study, three different simulations are carried out (see Table 1) driven by skewed and/or asymmetric flow. The oscillatory flow is driven by a prescribed horizontal pressure gradient f_i . To generate time-series of near-bed orbital velocity with prescribed values of velocity and acceleration skewness to drive the numerical simulations, the analytical formula proposed by Abreu et al. (2010) was used,

$$U_0(t) = U_t f \frac{\left[\sin(\omega t + \sigma_0) + \frac{r\sin(\varnothing)}{1 + \sqrt{1 - r^2}}\right]}{\left[1 - r\cos(\omega t + \varnothing + \sigma_0)\right]}$$
(1)

where U_1 is the amplitude of the wave orbital velocity, r is an index of nonlinearity (r=0 corresponds to linear wave orbital velocity), f is a function of r ($f=\sqrt{1-r^2}$), $\omega=2\pi/T$ is the angular frequency where T represents the wave period. Importantly, \varnothing is a waveform parameter varying from -90° to 0° ; $\varphi=-90^\circ$ corresponds to velocity skewed flow (VS) and $\varphi=0^\circ$ will produce an asymmetric flow (AS). To produce a combined asymmetric-skewed flow (AS-SK), φ should be in the range

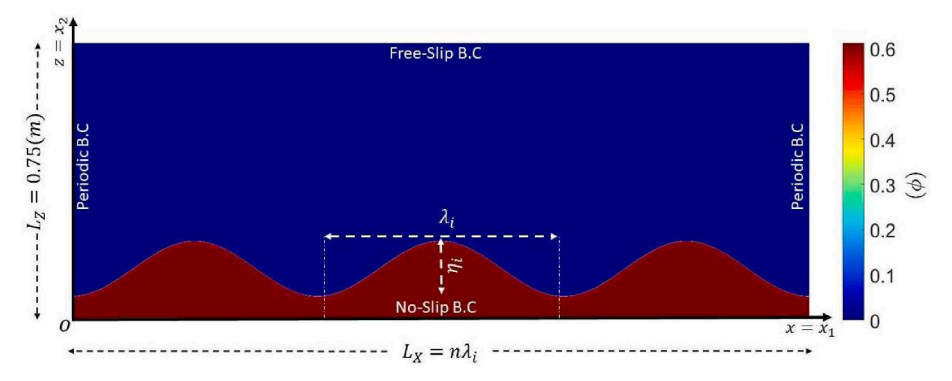


Fig. 2. Schematic plot of the model domain and initial ripple bed. The color bar shows the sediment volumetric concentration.

Table 1
A summary of the flow conditions of each case that was simulated in this study.

Case ID	T (s)	D ₅₀ (mm)	Umax (m/s)	Umin (m/s)	Urms (m/s)	r	Ø (rad)	σ_0	Ψ	Sk_{∞}	As_{∞}
AS	6.25	0.51	0.60	-0.60 -0.50 -0.50	0.42	0.30	0°	0°	42	0.00	0.66
VS	6.25	0.51	0.70		0.42	0.30	-90°	8°	42	0.33	0.00
AS-VS	6.25	0.51	0.70		0.42	0.60	-45°	13°	42	0.52	0.99

 $-90^{\circ}-0^{\circ}$. The phase shift σ_0 , is calculated such that the free-stream velocity becomes zero at t=0. In this study, the positive (negative) velocity represents onshore (offshore) directed flow.

The sediment size and flow conditions are summarized in Table 1 in which U_{max} , U_{min} and U_{rms} are the maximum, minimum and root mean square velocities, respectively. The mobility number in is defined as,

$$\psi = \frac{2U_{rms}^2}{(s-1)gD_{50}} \tag{2}$$

also, the velocity skewness parameter is formulated as

$$Sk_{\infty} = \langle U_{\infty}^3 \rangle / \langle U_{\infty}^2 \rangle^{1.5}$$
 (3)

and the asymmetry parameter is defined based on the flow acceleration (velocity gradient) as:

$$As_{\infty} = \langle \dot{U}_{\infty}^3 \rangle / \langle \dot{U}_{\infty}^2 \rangle^{1.5} \tag{4}$$

The pure onshore velocity-skewed flows have positive Sk_{∞} with zero As_{∞} , while the pure onshore acceleration-skewed flows have zero Sk_{∞} with positive As_{∞} . The values of Sk_{∞} and As_{∞} corresponding to the simulated flow conditions are also reported in Table 1.

T: Oscillatory wave period, D_{50} : sediment size, U_{max} : maximum velocity, U_{min} : Minimum velocity, U_{rms} : root-mean square velocity, r: nonlinearity measure, \emptyset : wave form parameter, σ_0 : phase shift, ψ : Mobility number, Sk_{∞} : Skewness parameter, As_{∞} : Asymmetry parameter, Case AS is designed to simulate the water tunnel experiment of an orbital ripple driven by an asymmetric oscillatory flow conducted by Yuan and Wang (2019) [Case ASY60a]. A detailed comparison between model results and measured data is analyzed for this case to validate the model. In the laboratory experiment, well-sorted coarse sand of a grain size $D_{50} = 0.51 \, mm$ with specific density s = 2.65 is utilized and the oscillatory flow period is T = 6.25s. More information about flow conditions is provided in Table 1. In case VS, the rms orbital velocity amplitude, wave period, and sediment size are kept the same as in case AS, except the flow is velocity skewed. In the same manner, both flow asymmetry and skewness are imposed in case AS-VS to investigate the sediment transport and ripple migration rate under combined oscillatory flows. Comparing the results for these cases will help to better understand the different wave-shape effects on the sediment transport over migrating ripples.

Recent studies (e.g., Scherer et al., 2022) showed that in order to correctly simulate the equilibrium ripple length from the flat bed, the simulation domain should be about 12 equilibrium ripple length which will be computationally demanding for the presented two-phase model. As the focus of the study is on the sediment transport over equilibrium ripple, the initial ripple length λ_i is set to be the same as the measured equilibrium ripple ($\lambda_e = 0.6m$) reported by Yuan and Wang (2019), following Salimi-Tarazouj et al. (2021a). The domain length is specified such that it includes n=3 ripples (i.e., $L_x=3\lambda_i=1.8m$, see Fig. 2). For the initial ripple height $\eta_i=0.15m$, we specify a much larger value than the measured ripple height which results in a large ripple steepness $(\eta/\lambda)_i = 0.25$. The domain height is set to be $L_z = 0.75m$ in all the simulations to ensure that the domain height is sufficiently large to cover the wave bottom boundary layer over the ripples. Salimi-Tarazouj et al. (2021b) showed that the final equilibrium ripple geometry (i.e., λ_f and η_f) is independent of the initial bed profile. The computational domain is discretized into $N_x = 3000$ uniform grids in the streamwise

direction with a grid length $\Delta x=0.6mm$. In the vertical direction, non-uniform grids of $N_z=580$ is used. By keeping the grid ratio near unity, $\Delta z\approx 0.6mm$ is used in the lower 0.2 m of the domain where a significant sediment transport takes place, and the vertical grid height is gradually increased away from the ripple bed to $\Delta z\approx 3mm$ at the top boundary. The same domain length and mesh discretization are used in VS and AS-VS cases as the same mobility number between these cases will result in similar ripple dimensions (Nielsen, 1981).

For each case, the simulation is conducted for 16 flow periods. In all cases, after 10 periods, ripples evolved into a more realistic shape (sharp crest and curved trough) and reached the quasi-steady state; the calculated wave-period-averaged net transport rate between two consecutive flow periods is less than 5 % and the migration rate is constant.

3. Model results

In this section, first, we will present the model results for ripples driven by the asymmetric flow (Case AS) and validate the model with the similar experiment conducted by Yuan and Wang (2019) (Case ASY60a). Simultaneously, by analyzing the model results for the skewed and combined cases, we aim at obtaining a more complete understanding of the flow-shape effect on sediment transport fluxes over migrating ripples.

3.1. Ripple geometry

In this study, the ripple's surface is defined as the sediment volumetric concentration $\varphi=0.57$ and the ripple crest and trough are determined by identifying the highest and the lowest points of the ripple profile. The volumetric concentration of 0.57 was selected because it corresponds to the theoretical random loose packing concentration for uniform spheres. Based on the model's results, minor variations in the critical concentration (e.g., using 0.55 or 0.59) are not expected to have a significant impact on the resulting ripple profile. The ripple length can be determined from the horizontal distance between two adjacent crests

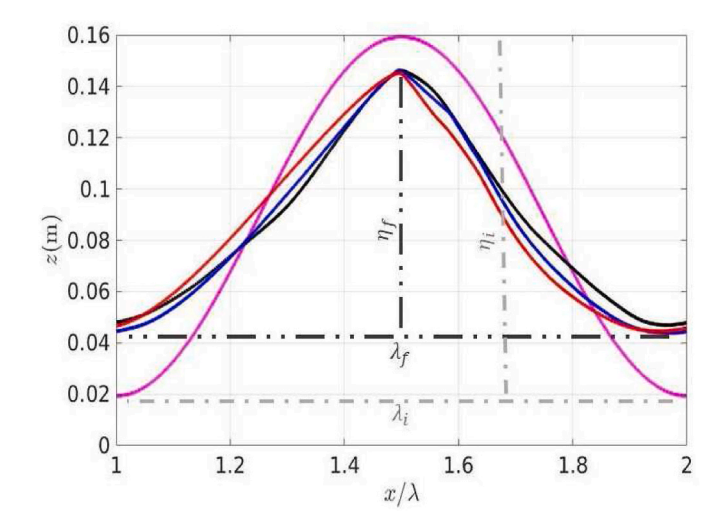


Fig. 3. Modeled middle ripple profile at final equilibrium contrasted with initial ripple profile (magenta line) for Case AS (black line), VS (blue line), and AS-VS (red line).

and the ripple height is defined as the vertical distance between the crest and the trough. Fig. 3 shows the period-averaged (time-averaged over the last wave period) ripple profiles for the middle ripple in the model domain along with the initial ripple profile (magenta profile) for the three cases studied. The modeled ripple height for the asymmetric flow (black profile in Fig. 2) is $\eta_f \approx 0.11m$, which gives a ripple steepness of $(\eta/\lambda)_f=0.183$ and it is in good agreement with the measured data reported by Yuan and Wang (2019) (see λ_m and $(\eta/\lambda)_m$ in Table 2). Model results show the same ripple dimensions for two other cases. As the mobility number is the same between all three cases, similar ripple dimensions are expected (Nielsen, 1981). Yuan and Wang (2019) reported a fairly symmetric ripple shape about the ripple crest with a small hump in the trough locations for highly asymmetric flows. However, Fig. 3 shows an asymmetric ripple shape for all three cases with the lee flank steeper compared to the stoss flank. The absolute value of the bed slope (see Fig. 4) increases from the trough location ($\beta = 0$) to a maximum value close to the ripple's crest over each ripple flank and reduces to a small value at the location of the ripple's crests. For the asymmetric flow (black dash-line in Fig. 4), the maximum bed slope over the stoss flank is $eta_{
m stoss} = 28^{
m o}$, while on the lee side it is $eta_{
m lee} = 31^{
m o}$. However, the maximum bed slope difference between the stoss and lee flank is significantly larger for the skewed (see blue solid line in Fig. 4) and the combined (red solid line in Fig. 4) flows ($eta_{lee} - eta_{stoss} = 12^{\circ}$). Fig. 4 indicates that the equilibrium ripple profiles show a steeper slope on the lee side, which is consistent with the direction of ripple migration. The ripple shape's asymmetry is more significant when driven by the skewed flow.

 λ_i and $(\eta/\lambda)_i$: Initial ripple length and steepness, respectively. Similarly, the subscripts f and m represent the final equilibrium ripple profile of the present numerical model and measured ripple geometry reported by Yuan and Wang (2019). $< Q_s >_{tx}$: Time- and ripple-averaged net suspended sediment transport rate. Similarly, the subscripts b and t represent the near-bed load and total net transport rates. V_m : ripple migration speed

3.2. Time-dependent fields

Yuan and Wang (2019) measured the detailed two-component velocity flow field, net sediment transport, and ripple migration rate. Hence, first, we compare streamwise velocity profiles at five different horizontal locations over the middle ripple at eight different time instances (see Fig. 5). To better relate the flow field to the sediment transport fluxes over the ripple, Fig. 6 is presented for those eight time instances, as well. In Figs. 5 and 6, the top panel shows the time series of free-stream velocity, which also signifies those time instances for which the comparisons between model results and experimental data are conducted. Following Salimi-Tarazouj et al. (2021a), Fig. 6 is organized to show the sediment concentration and velocity (left panels) fields, normalized vorticity field $[\Omega/\omega = \frac{1}{\omega} \left(\frac{\partial \omega^r}{\partial x} - \frac{\partial u^r}{\partial z}\right)]$ (middle panels), and nondimensional horizontal sediment flux $\left[\Psi = \frac{q}{\sqrt{(s-1)gD_{50}^3}}\right]$ (right panels, in which the horizontal sediment flux is written as $q = \varphi u^s$).

In Fig. 5, the vertical variation of velocity profiles shown here are due to complex vortex generation, ejection, and local flow acceleration over ripple (Salimi-Tarazouj et al., 2021a) and the numerical model can reproduce these key flow features with good agreements when compared with measured data. The results of the analysis show a strong

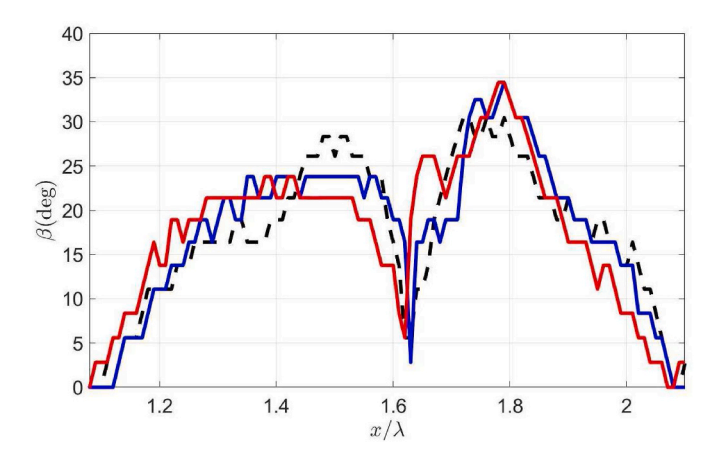


Fig. 4. Modeled middle ripple bed slope at final equilibrium state for Case AS (black dash-line), VS (blue line), and AS-VS (red line). The crest locations are shifted horizontally for better comparison.

agreement between the model results and the experimental data, as indicated by the computed correlation coefficient ($R^2 = 0.892$) and the root-mean-square error (E = 00 074 m/s). During the off-onshore flow reversal a vortex dipole is formed (see the middle panel in Fig. 6a); a primary vortex (with positive vorticity) and a strip of negative vorticity underneath it in the local shear layer where a secondary vortex forms with time due to the adverse pressure gradient along the ripple's surface (Onder and Yuan, 2019). The stoss primary vortex is detached from the secondary vortex formed on the lee side (positive vorticity) during the offshore half cycle (follow middle panels in 6e-6h); similarly, the stoss secondary vortex (negative vorticity) is the nucleus of the lee side primary vortex (follow middle panels in 6a-6d). The vortex dipole has produced a strong jet on the stoss side, which forces the cloud of sediment suspended and advected via the primary vortex toward the onshore direction over the ripple crest (see the left panel in 6a). Meanwhile, accelerated flow over the ripple's surface causes an onshore near-bed load flux all over the ripple's surface (see the right panel in 6a).

During the onshore acceleration phase, the stoss primary vortex has passed the ripple's crest while its strength is reduced (see the middle panel in 6b); the boundary shear layer (negative vorticity close to the ripple's surface) is extending from the stoss flank over the ripple's crest. The cloud of sediment trapped in the stoss primary vortex has passed the ripple's crest at this moment (see the left panel in 6b). Very close to the bed, the near-bed load onshore flux is intense over the stoss flanks while the eroding sediment over the stoss flank is feeding the intense onshore sediment flux over the ripple's crest (see the right panel in 6b).

When the onshore free-stream velocity reaches its peak value, on the stoss side, the boundary layer is attached to the ripple's surface, and the near-bed flow is forced to accelerate toward the ripple crest with an evident overshoot velocity feature, which is the largest on the ripple crest. At this time, two vortex structures exist over the ripple (see the middle panel in 6c); the strong flux of negative vorticity produced on the stoss flank is feeding the growing negative lee primary vortex; the weak positive vortex structures over the stoss flank higher in the water column are the residual vortices traveled from the adjacent offshore ripple produced during the previous offshore half cycle. Meanwhile, there are two clouds of sediment over the ripple (see the left panel in 6c); a dense

Table 2A summary of the model results for ripple dimension, net transport rates, ripple migration, and measured ripple dimension.

Case ID	λ_i (m)	$\left(\frac{\eta}{\lambda}\right)_i$	λ_f (m)	$\left(\frac{\eta}{\lambda}\right)_f$	λ_m (m)	$\left(\frac{\eta}{\lambda}\right)_m$	$< Q_s>_{tx} (m^2/s) \ imes 10^{-6}$	$< Q_b>_{tx} (m^2/s) \ imes 10^{-6}$	$< Q_{tm}>_{tx} (m^2/s) imes 10^{-6}$	$V_m \ (mm \ /min)$
AS	0.60	0.25	0.60	0.183	0.605	0.18	6.60	14.20	20.80	24
VS	0.60	0.25	0.60	0.183	_	-	-13.70	10.00	-3.70	17
AS-VS	0.60	0.25	0.60	0.182	-	-	-0.80	19.40	18.60	31

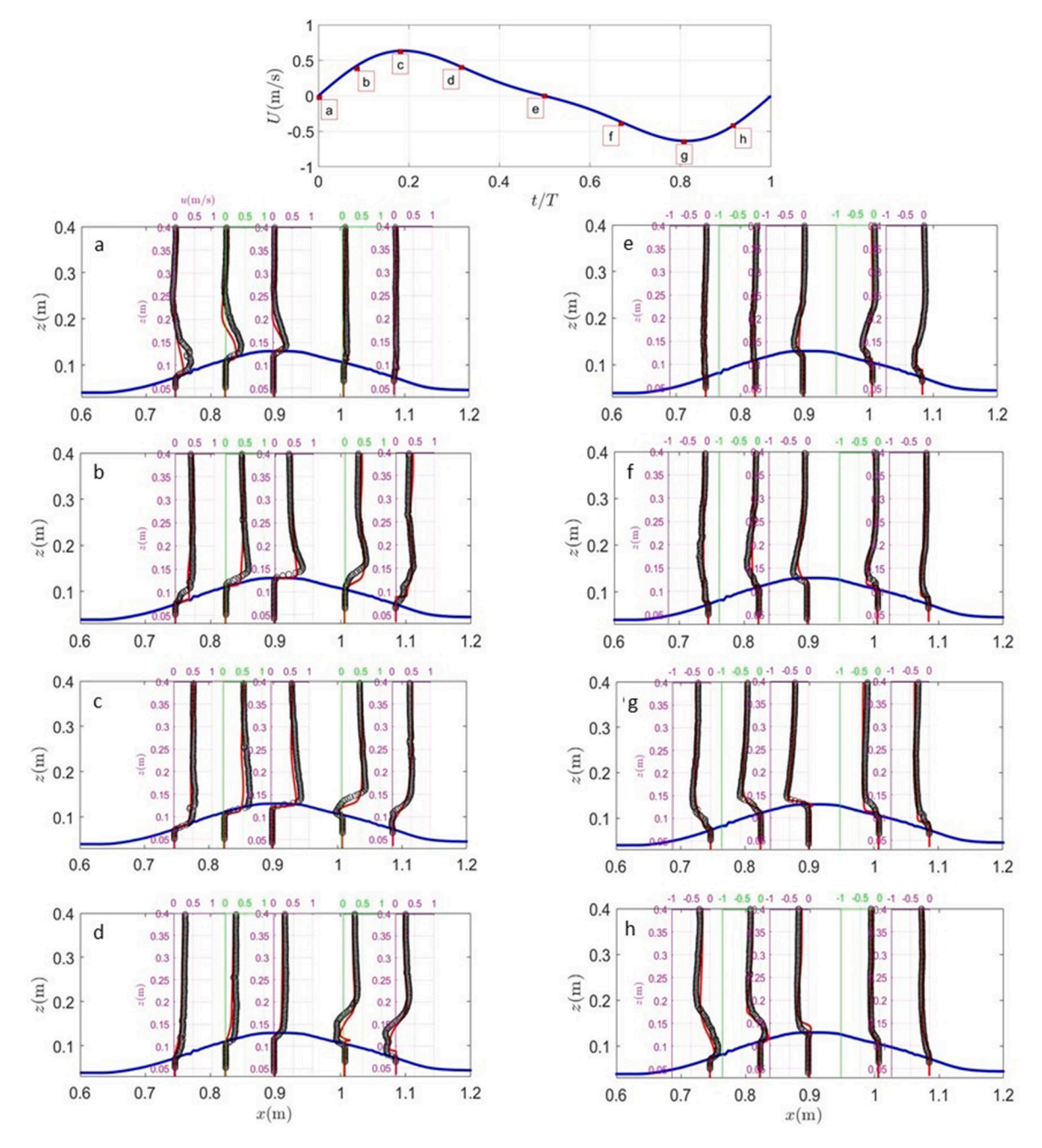


Fig. 5. Comparison of the streamwise fluid velocity at eight different instances (panel (a) to (h)) between model results (solid curves) and measured data (symbols), for case AS. Each panel shows velocity profiles at five locations over the ripple. The top panel presents the time-series of free-stream velocity with different instances shown in panel (a) \sim (h) indicated.

cloud over the crest and lee flank with high sediment concentration near the ripple's surface and a cloud of sediment approaching the ripple from the offshore side which is produced due to the stoss vortex generation over the adjacent offshore ripple. The onshore near-bed load from the stoss side continues to feed the cloud of the sediment and deliver the sediment over the ripple crest to the lee side. Meanwhile, the near-bed load over the lee side away from the ripple crest is reduced significantly because the flow close to the ripple's surface starts to reverse (see the right panel in 6c).

During the onshore-deceleration phase, Fig. 6d shows the lee primary vortex (with negative vorticity) is growing in size and strength and a strip of positive vorticity (attached to the lee flank) emerges within the returning boundary layer flow induced by the primary vortex. Meanwhile, the primary vortex is still attached to the ripple's crest with the

edge of negative vorticity extended over to the stoss side of the adjacent ripple at the onshore side (see the middle panel in 6d). A dense cloud of sediment is formed due to the primary vortex generation over the lee flank, while another cloud of the sediment is approaching the ripple from the second adjacent ripple located in the offshore direction (see the left panel in 6d). The near-bed load consists of an onshore directed flux at the ripple crest, which continues to deliver the eroded sediment from the stoss flank to the lee side (and lee primary vortex). Meanwhile, an offshore directed flux is produced by the lee vortex-induced (returning) boundary layer flow. Importantly, an onshore-directed near-bed sediment flux due to avalanching (Salimi-Tarazouj et al., 2021a) is limiting this offshore-directed near-bed load over the lee flank (see the right panel in 6d).

Comparing the on-offshore (Fig. 6e) and off-onshore (Fig. 6a) flow

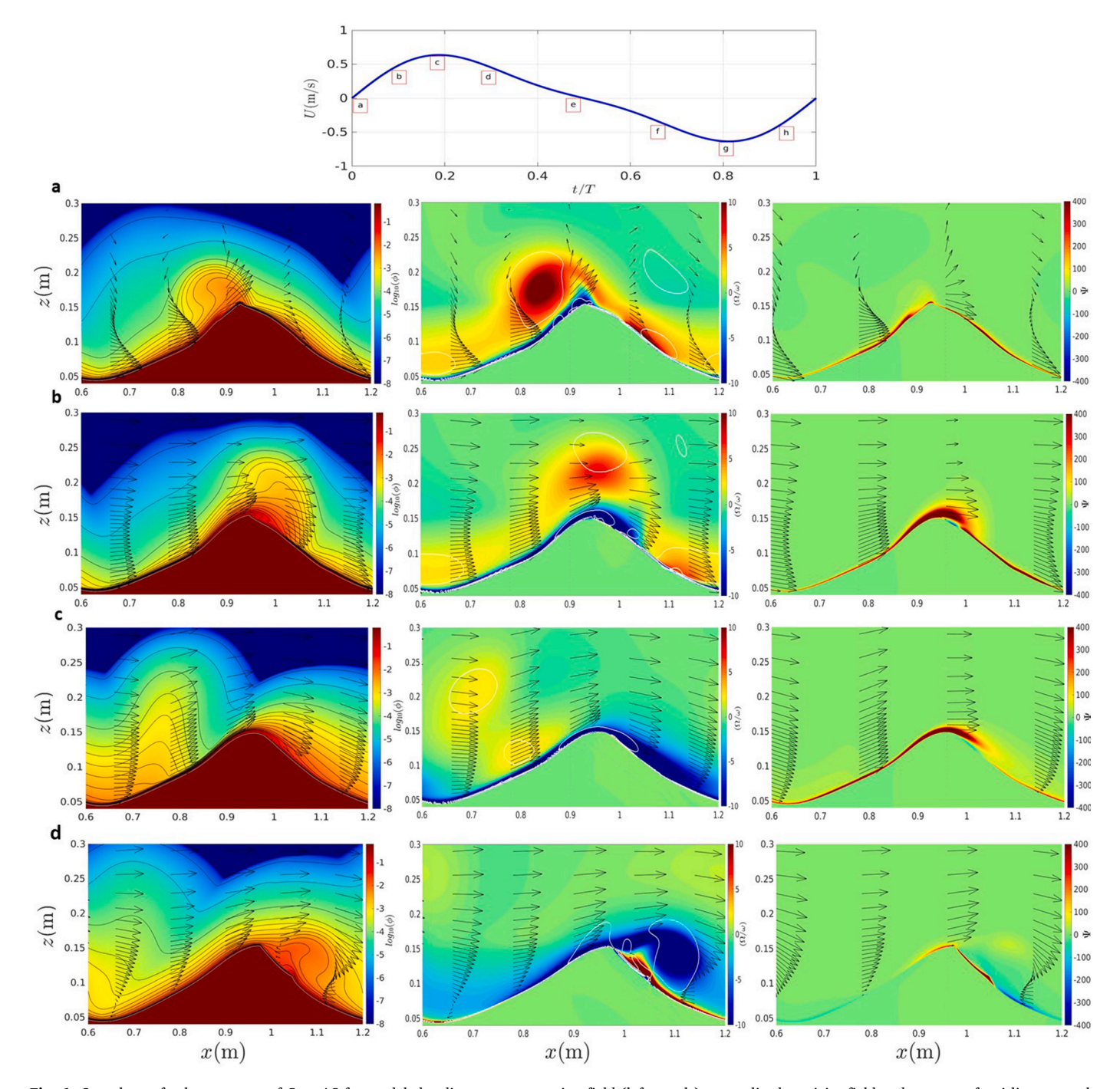


Fig. 6. Snapshots of color contours of Case AS for modeled sediment concentration field (left panels), normalized vorticity field and contour of swirling strength (white contour) (middle panels), and sediment horizontal flux (right panels) for eight instances (a)~(h) during a wave period. In each panel, the velocity field is down-sampled and represented by the vectors. The top panel shows the time-series of free-stream velocity and the corresponding eight instances are indicated.

reversals reveals important differences. The primary vortex over the lee side is of less strength compared to the primary vortex over the stoss side (compare the middle panels in Fig. 6e and a, respectively). Although the cloud of suspended sediment over the lee side (left panel in Fig. 6e), is slightly larger than the one over the stoss flank (left panel of Fig. 6a), the onshore near-bed load at the time of the off-onshore flow reversal (right panel in Fig. 6a) is clearly greater than the near-bed load during the onoffshore flow reversal (right panel in Fig. 6e). The larger near-bed load during off-onshore flow reversal is due to higher accelerating flow. Moreover, the weak offshore near-bed load is still limited by the onshore sediment avalanching over the lee flank (right panel of Fig. 6e).

The difference between the offshore and onshore accelerations phases is significant in Fig. 6f and b, respectively. Compared to the stoss primary vortex, during the onshore acceleration phase, the lee primary vortex strength is significantly reduced during the offshore acceleration phase and, more importantly, it has not yet passed the ripple crest (compare the middle panels in 6f and 6b), meaning that the lee primary vortex has large residence time over the lee flank before traveling to the opposite side compared to the stoss primary vortex. Consequently, suspended sediment trapped in the lee primary vortex has more time to settle down before getting advected over the ripple crest toward the offshore direction. As a result, the cloud of suspended sediment passing

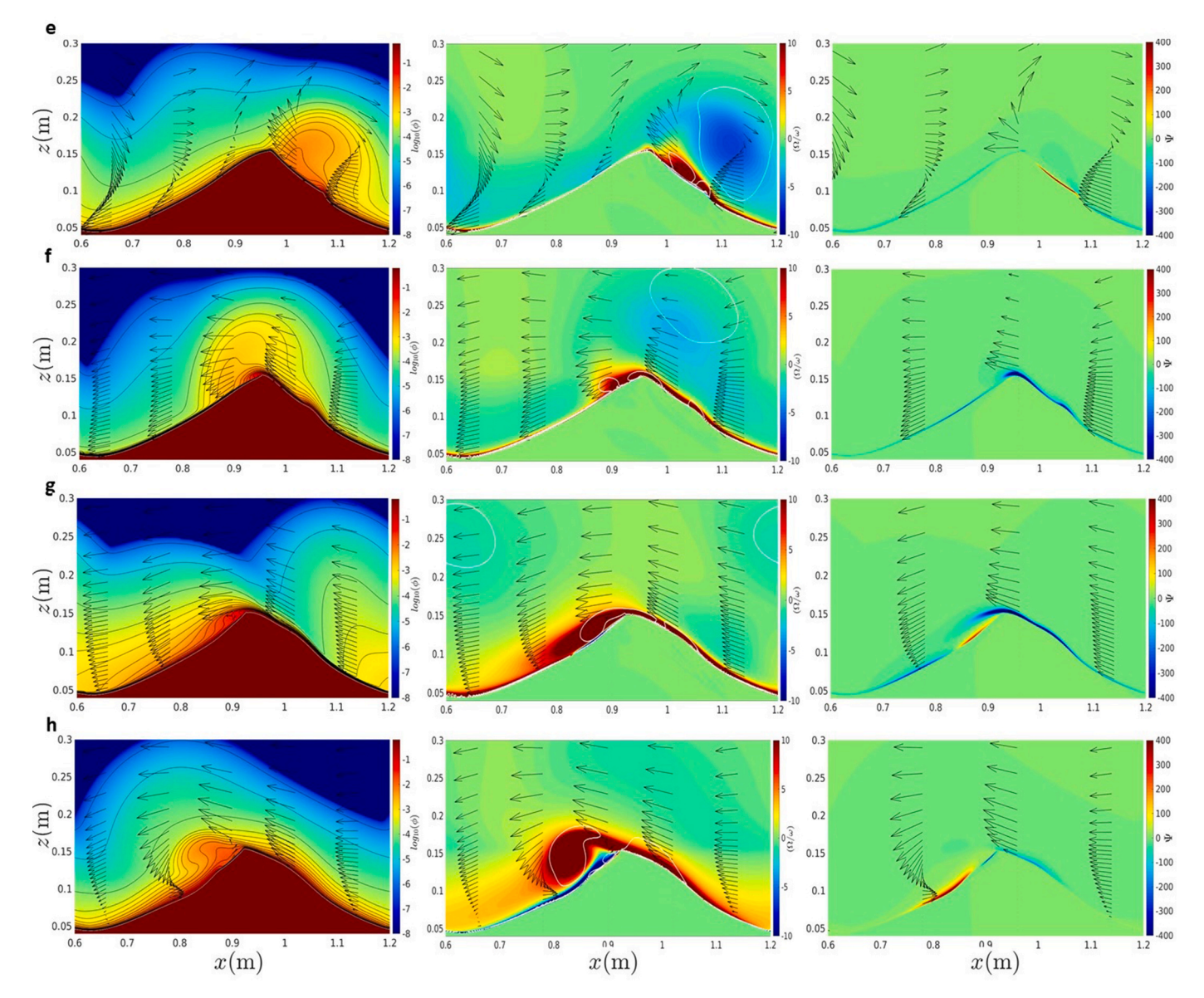


Fig. 6. (continued).

the ripple crest toward the offshore side is more diluted compared to the one passing the ripple crest during the onshore acceleration phase (compare the left panels in 6f and 6b). The near-bed load is offshore directed over the ripple's surface; however, the magnitude is significantly smaller compared to the onshore directed near-bed load during the onshore acceleration phase (compare the right panels in 6f and 6b).

During the offshore flow peak (Figs. 5g & 6g) and deceleration phase (Figs. 5h & 6h), the flow field and sediment flux structures are qualitatively similar to those shown in Figs. 5c, 6c and 5d and 6d during the onshore flow, respectively. However, there are several important differences in their magnitudes. Notably, the near-bed velocity approaching the ripple crest shows a weaker overshoot during the offshore flow peak compared to the onshore flow peak (compare Fig. 5g and c). For instance, the maximum overshoot velocity over the ripple crest is about 0.83 m/s during the onshore flow peak (see the velocity profile at x = 0.9m in Fig. 5c) while it is 0.64 m/s during the offshore flow peak (see the velocity profile at x = 0.9m in Fig. 5g). Therefore, the flow asymmetry causes a higher boundary layer shear (vorticity) on the stoss flank and the ripple crest during the onshore flow phase. Fig. 6g shows that the residual primary lee vortex is smaller compared to the residual primary stoss vortex while the vortex structure attached to the ripple's

surface has a similar feature as the one during the onshore flow peak (compare the middle panels in 6g and 6c). Contrary to the phase of the onshore flow peak, the offshore suspended and near-bed load sediment fluxes above the ripple are weaker during the offshore flow peak (compare the left and right panels in 6g and 6c). However, a strong onshore near-bed load flux is formed on the stoss flank due to the stoss vortex-induced boundary layer returning flow (see the right panel in 6g). Moreover, during the offshore deceleration phase, there is no cloud of suspended sediment over the lee flank while the cloud of sediment, traveling from the adjacent offshore ripple, is approaching the middle ripple from the stoss flank during the onshore deceleration phase (compare the left panel in 6h and 6d). Furthermore, the offshore sediment avalanching flux on the stoss flank is weaker than the onshore sediment avalanching on the lee flank (compare the right panel in 6h and 6d) as the avalanching flux has less time to develop on the stoss flank due to the faster stoss vortex generation-ejection.

In summary, the model generally predicts key flow and sediment flux features above the ripple, showing good agreement with measured data for flow velocity. However, it slightly underestimates near-bed velocity, particularly on the stoss side (Fig. 5a) and lee side (Fig. 5d), attributed to limitations in the k- ϵ closure method (Salimi-Tarazouj et al., 2021a).

Figs. 5 and 6 reveal that asymmetric flow results in higher near-bed velocity and sediment flux on the stoss flank and ripple crest during onshore flow compared to the lee flank during offshore flow, aligning with the findings of Yuan and Wang (2019) regarding boundary layer thickness and shear skewness. Additionally, flow asymmetry induces a strong stoss vortex generation-ejection, leading to greater onshore suspended sediment flux through a phase-lag effect, which is more pronounced than in flat-bed sheet flows (Ruessink et al., 2011).

For orbital ripples driven by a skewed oscillatory flow, Salimi-Tarazouj et al. (2021a) confirmed the net offshore directed suspended load due to the phase-lag effect (contrary to the flow asymmetry-induced phase-lag effect) and the net onshore directed near-bed load via ripple

migration. Hence, the main purpose of presenting the model results here for the skewed flow (VS) is to reveal the difference with respect to the asymmetric flow (AS). Fig. 7 shows the model results for case VS, at four key time instances, when major differences in vortex generation-ejection process and sediment fluxes exist (e.g., Fig. 7b and d). Comparing the off-onshore and on-offshore flow reversal time instances (Fig. 7a and c) reveals major differences. The lee primary vortex as well as the sediment cloud are larger and stronger than those over the stoss side (compare the middle and left panels in 7a and 7c). As a result, the cloud of suspended sediment passing the ripple's crest toward the offshore at the time of the on-offshore reversal is greater than the cloud of sediment passing the ripple's crest toward the onshore flow reversal

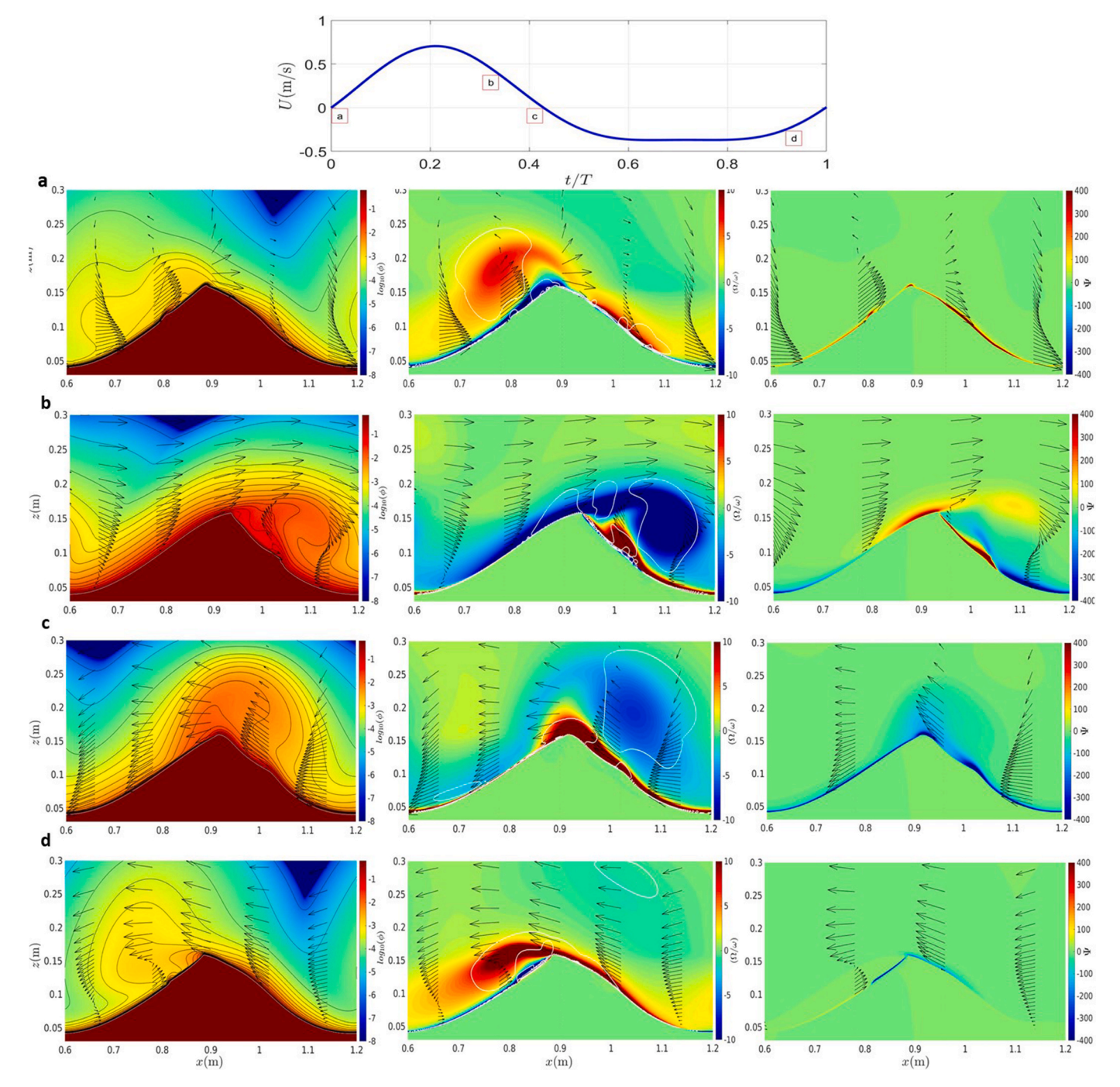


Fig. 7. Snapshots of color contours of Case VS for modeled sediment concentration field (left panels), normalized vorticity field and contour of swirling strength (white contour) (middle panels), and sediment horizontal flux (right panels) for four instances (a) ~(d) during a wave period. In each panel, the velocity field is down-sampled and represented by the vectors. The top panel shows the time-series of free-stream velocity and the corresponding eight.

(compare the left panels in 7a and 7c). Hence, the phase-lag effect (due to the strong lee vortex generation-ejection process) causes a net offshore directed suspend load, under the skewed flow (see Salimi-Tarazouj et al. (2021a) for more details of a similar case). During the onshore deceleration phase, the near-bed load consists of onshore sediment erosion on the stoss flank and offshore sediment flux due to the vortex-induced returning flow on the lee side, which is limited by the onshore sediment avalanching (see the right panel in 7b); the same near-bed load structure is formed during the offshore deceleration phase but the flux intensities are weaker (compare the right panel in 7b and 7d). Comparing the near-bed load fluxes during onshore deceleration and on-offshore flow reversal phases, between the asymmetric and

skewed flow, show that the strong lee vortex formation under the skewed flow generates greater offshore directed vortex-induced returning flux compared to that under the asymmetric flow (compare the right panels in Fig. 6d and e and 7b,c). Due to the larger offshore flux driven by the returning flow, a large amount of sediment is pushed toward the ripple crest on the lee flank by the skewed flow. This will increase the lee flank's slope which makes it harder for the eroded sediment to pass the ripple crest. As a result, a strong onshore sediment avalanching occurs on the lee flank. The difference in the near-bed load fluxes during the offshore deceleration phase (right panels in Figs. 6h and 7d) are even more evident; under the asymmetric flow, the onshore directed stoss vortex-induced returning flux is greater (due to the strong

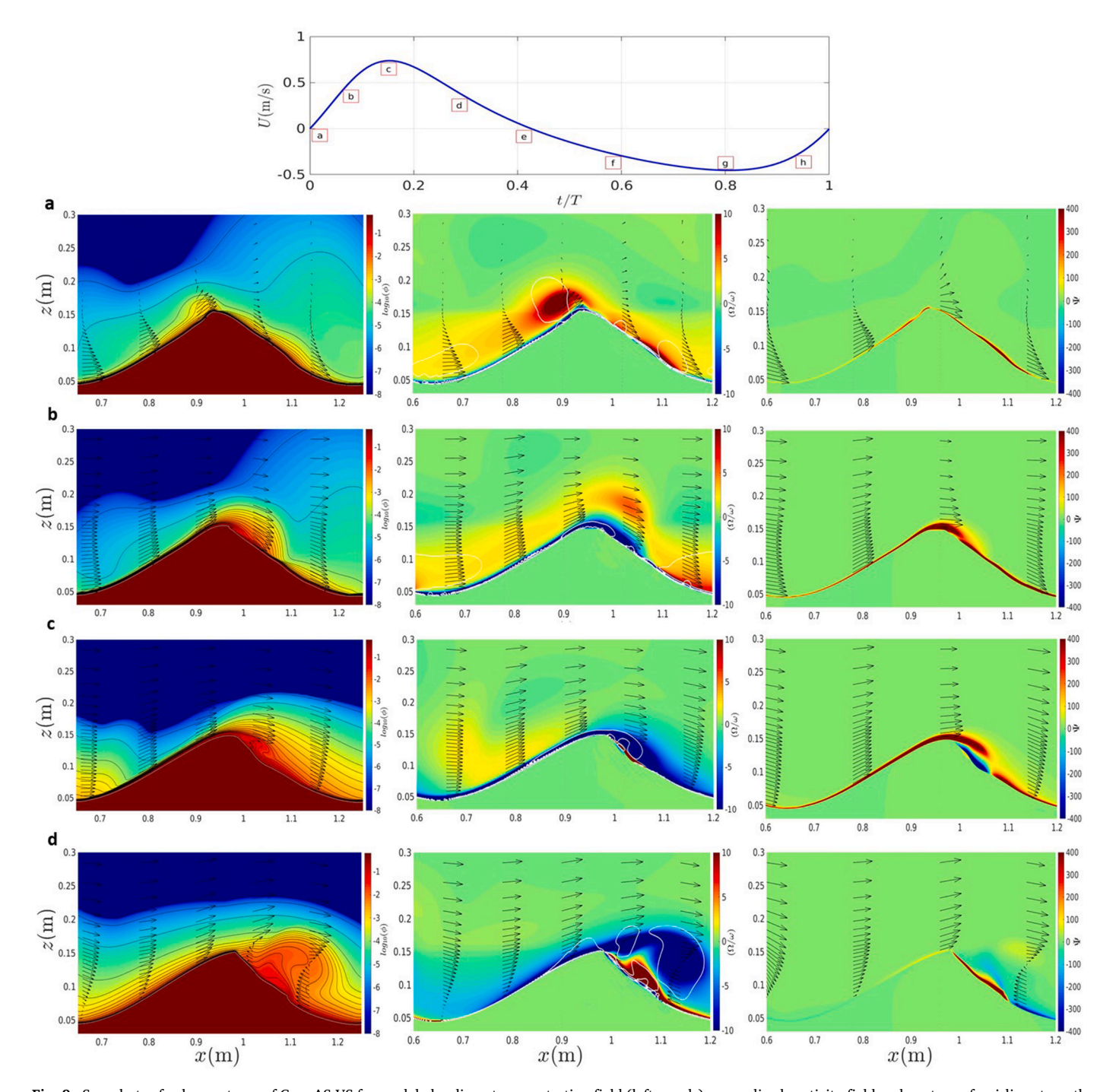


Fig. 8. Snapshots of color contours of Case AS-VS for modeled sediment concentration field (left panels), normalized vorticity field and contour of swirling strength (white contour) (middle panels), and sediment horizontal flux (right panels) for eight instances (a)~(h) during a wave period. In each panel, the velocity field is down-sampled and represented by the vectors. The top panel shows the time-series of free-stream velocity and the corresponding eight.

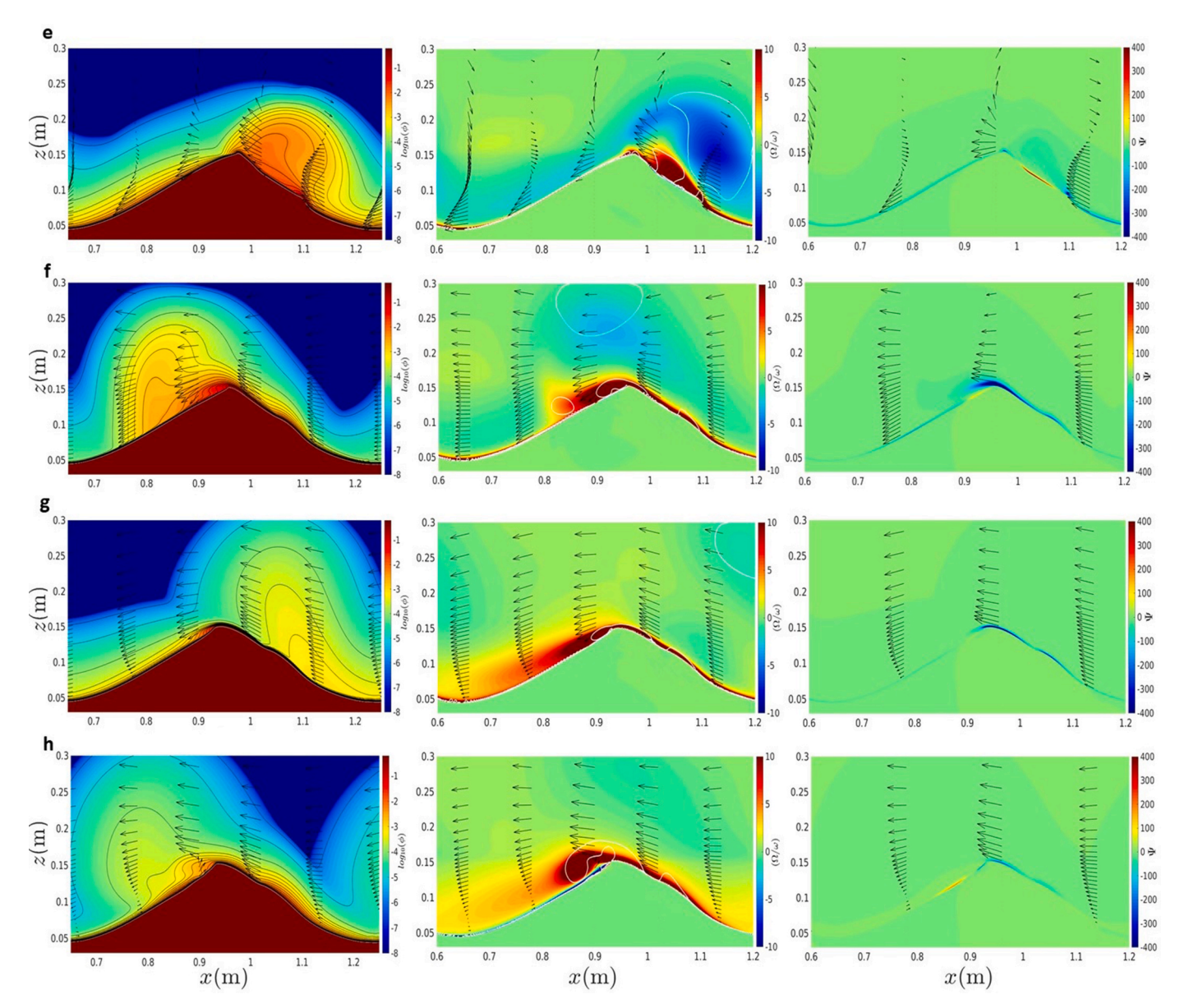


Fig. 8. (continued).

stoss vortex generation), furthermore, the offshore sediment avalanching on the stoss flank is reduced (due to fast stoss vortex ejection), compared to the skewed flow. This signifies the pronounced onshore transport during off-onshore flow reversal (positive phase lag effect) for the asymmetric flows.

In Fig. 8, model results are presented for the case AS-VS for the temporal evolution of sediment concentration, normalized vorticity, and sediment horizontal flux. Similar to the skewed flow, the primary vortex (with positive vorticity in the middle panel of Fig. 8a) above the stoss side at the off-onshore reversal is smaller than the one above the lee side at the on-offshore flow reversal (with negative vorticity in the middle panel of Fig. 8e). The cloud of suspended sediment over the lee flank is greater than that over the stoss flank due to more intense lee vortex generation-ejection process during onshore cycle. More suspended sediments pass the ripple crest toward the offshore during the offshore acceleration phase (left panel of Fig. 8f) compared to those passing the ripple's crest toward the onshore side during the onshore acceleration phase (left panel in Fig. 8b). However, the difference between the onshore and offshore acceleration phases appears to be weaker compared to that of skewed (VS) flow. The main difference in the

sediment field is during the onshore and offshore velocity peaks; at the time of the onshore flow peak, the onshore suspended sediment flux. mainly over the lee flank, is larger compared to the cloud of sediment over the ripple at the time of offshore flow peak which is traveling toward the offshore direction (compare the left panels in 8c and 8g). During the onshore half flow-cycle, the near-bed load is mostly onshore directed and greater than the offshore directed near-bed load sediment flux during the offshore half-cycle (compare the right panels in Fig. 8a-c to 8e-g); the onshore sediment avalanching flux and offshore lee vortexinduced returning sediment flux on the lee flank during the onshore deceleration phase (right panel in Fig. 8d) are greater than those on the stoss flank during the offshore deceleration phase (right panel in Fig. 8h). Hence, a net onshore directed near-bed load is expected in the combined flow due to larger velocity and acceleration during onshore flow. However, the magnitude of the net offshore suspended load (or even the direction), depends on the strength of the phase-lag effects due to the skewness (inducing offshore flux) and the asymmetry (inducing onshore flux). A more thorough analysis on net sediment flux is presented in the next section.

Coastal Engineering 189 (2024) 104470

3.3. Averaged fields

To show the asymmetry in the sediment horizontal fluxes, the timeand ripple-averaged ($<>_{tx}$) sediment flux profiles are presented in Fig. 9. The shaded region shows the area below the elevation of two grains diameter $(2D_{50})$ above the ripple crest for case AS (the difference in crest location is within $4D_{50}$ for different cases). As it is shown in Figs. 6–8 (right panels), near the ripple's surface, sediment transport occurs via sediment erosion in the boundary layer over the ripple flank, sediment avalanching, and the sediment flux due to the vortex-induced returning flow. To include the sediment transport fluxes associated with these mechanisms in the near-bed load transport rate, it is calculated via a bathymetric-following method, which accounts for the transport from the bottom of the domain to the vertical location z_{so} which is 20 D_{50} above the ripple's surface (i.e., $z_{so} = z(\varphi = 0.57) + 20D_{50}$). Based on our analysis, the volumetric concentration at this specific location stands at approximately $\varphi = 0.08$. It's worth noting that a volume concentration of 0.08 is a commonly used threshold in earlier sediment transport studies for distinguishing between suspended load and near-bed load (e. g., Bagnold, 1966; Dohmen-Janssen and Hanes, 2002; Lanckriet and Puleo, 2015). This choice aligns with the approach employed by van der Werf et al. (2007), where sensors to measure the suspended load were positioned 10 mm (approximately 20 D_{50}) above the ripple, closely following its shape. Hence, the near-bed load transport rate at a given location (x) is calculated as,

$$Q_b = \int_{z=0}^{z=z_0} q(z)dz \tag{5}$$

The suspended load transport rate is then defined as transport above $z=z_{s0}$ to the top of the model domain:

$$Q_s = \int_{z=-\infty}^{z=L_z} q(z)dz \tag{6}$$

The total transport rate at a given location (Q_{tm}) is consequently the summation of the near-bed load and suspended load transport rate (i.e., $Q_{tm} = Q_b + Q_s$). The time series of ripple (x)-averaged transport rates for the asymmetric, skewed, and combined flows over one period are shown in Fig. 10 a, b, and c, respectively. The top panel in Fig. 10 shows the normalized free-stream velocity for each case.

For the asymmetric flow (black dash-line in Fig. 9), the onshore (positive) flux is found throughout the entire vertical domain. The

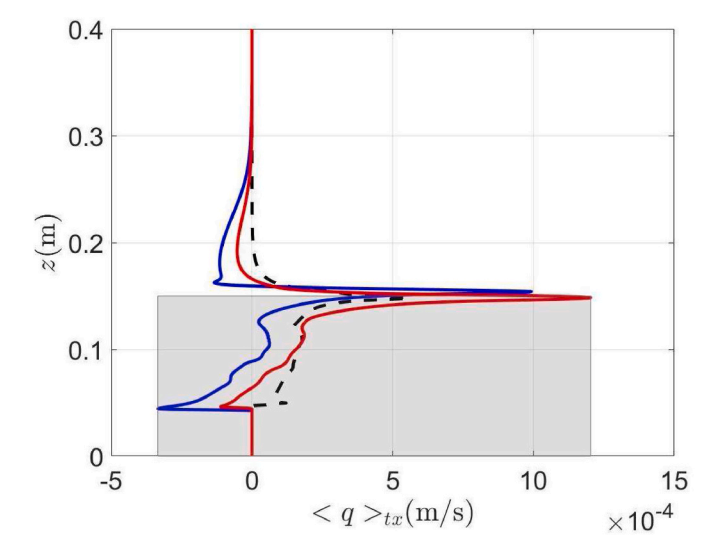


Fig. 9. Streamwise (ripple)-averaged and time-averaged sediment flux profile for Case AS (black dash-line), Case VS (blue solid line), and Case AS-VS (red solid line). The gray region shows the region below $2D_{50}$ above the Case ASY's crest location.

positive suspended load above the ripple's crest is due to the positive phase-lag effect induced by the faster and stronger stoss vortex generation-ejection. Under the ripple's crest, the positive sediment flux is mainly due to the asymmetric near-bed sediment flux resulting from larger acceleration due to onshore flow cycle. By integrating the wave period- and ripple-averaged sediment flux vertically, the modeled total net transport rate $\langle Q_{tm} \rangle_{tx} = 20.8 \times 10^{-6} m^2/s$ is obtained which is in good agreement with the measured net transport rate $\langle Q_{te} \rangle_{tx} =$ $20.6 \times 10^{-6} m^2/s$ reported by Yuan and Wang (2019). Fig. 10a shows that during the onshore half-cycle, ripple-averaged total transport rate (black solid line), near-bed load transport rate (red solid line), and suspended load transport rate (blue dash line) are onshore directed, and their values are greater than those during the offshore half cycle. The contribution of the near-bed load is greater than the suspended load (compare the red solid line to the dash blue line in 10a). Larger suspended load during the onshore half-cycle (due to the phase-lag effect) compared to the offshore half-cycle results in a net (time- and ripple-averaged, $\langle \rangle_{tx}$) onshore-directed suspended load transport rate $\langle Q_s \rangle_{tx} = 6.6 \times 10^{-6} m^2/s$. The imbalance of the near-bed load transport rate between two flow half-cycle is even larger which causes a large net on shore near-bed load transport rate $< Q_b>_{tx} = 14.2 \times 10^{-6} m^2/s$.

The time- and ripple-averaged sediment flux profile for the skewed flow (blue solid line in Fig. 9) reveals important differences between this case and the asymmetric flow (black dash-line). Above the ripple's crest level, the sediment flux is offshore-directed and in terms of magnitude, it is larger compared to that of the asymmetric flow. Under the ripple's crest, between z = 0.09-0.16 m, the sediment flux is directed onshore. The peak onshore sediment flux at the ripple crest is greater for the skewed flow than that of the asymmetric flow, which is due to the larger onshore velocity peak in the onshore skewed flow. Contrary to the asymmetric flow, under the ripple's crest between z = 0.04-0.09 m, the flux is offshore directed which is associated with the lee vortex returning flow. Later, we will present a more detailed analysis of this complex near-bed load flux pattern. The modeled total net transport rate $< Q_{tm}>_{tx} = -3.70 \times 10^{-6} m^2/s$ is offshore directed but the magnitude is smaller compared to the asymmetric flow case. Fig. 10b indicates that during the onshore flow acceleration period, the near-bed load transport (red solid line in Fig. 10b) is the dominant component until just passing the onshore peak flow. During the subsequent onshore flow deceleration phase, the primary vortex is sufficiently large to trap and transport a considerable amount of suspended load comparable to the near-bed load. During offshore flow acceleration and approaching the time of offshore flow peak, the suspended load is clearly dominant which is due to the strong vortex generation-ejection process. The near-bed load transport rate during the onshore half-cycle is greater than the offshore half-cycle. However, the suspended load transport rate is larger during the offshore half-cycle. Consequently, the net offshore directed suspended load transport rate $\langle Q_s \rangle_{tx} = -13.70 \times 10^{-6} m^2/s$ is greater than the net onshore directed near-bed load transport rate $\langle Q_b \rangle_{tx} =$ $10 \times 10^{-6} m^2/s$.

Combining the asymmetry and the skewness reduces the offshore directed suspended flux above the ripple's crest (see the red solid line in Fig. 9); the asymmetry-induced positive phase-lag effect (causing an onshore flux) reduces the skewness-induced offshore directed suspended flux due to the negative phase-lag effect. Importantly, the peak onshore directed sediment flux around the ripple's crest is even larger than that of the skewed flow and it is twice the asymmetric flow's peak value (compare the red solid line to the black dash-line in Fig. 9). This is due to combining the skewness and asymmetry, both increasing onshore transport in the near-bed load. The returning flow induces offshore sediment flux (z = 0.04–0.06 m) underneath the strong lee vortex, but the intensity is small compared to the skewed flow. The total net transport rate $< Q_{tm} >_{tx} = 18.60 \times 10^{-6} m^2/s$ is onshore directed and it is slightly smaller than the asymmetric flow due to the negative phase-lag effect in suspended load and larger returning flow driving offshore

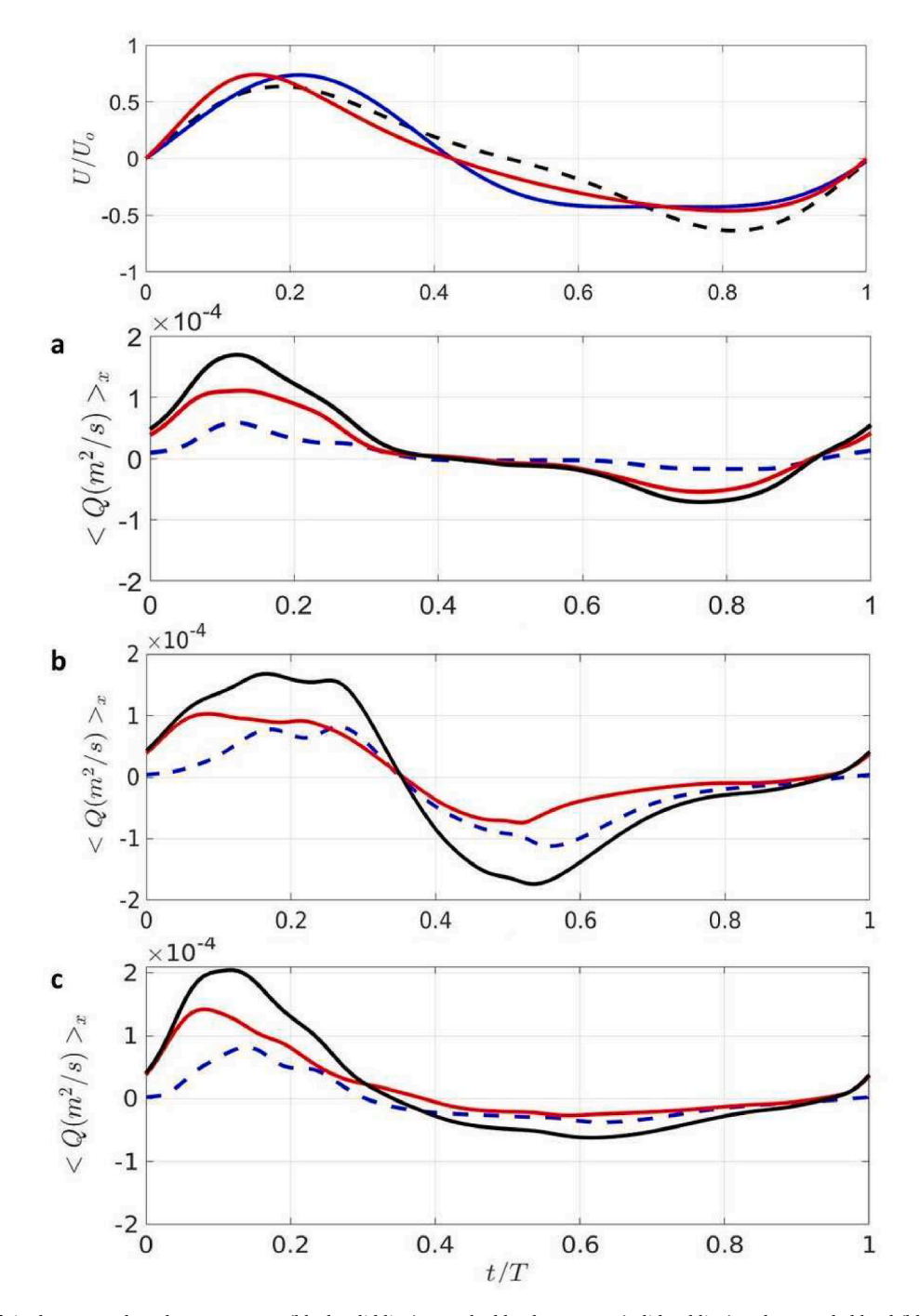


Fig. 10. Time series of ripple-averaged total transport rate (black solid line), near-bed load transport (solid red line) and suspended load (blue dash-line) and for (a) Case AS, (b) Case VS, and (c) Case AS-VS. The top panel shows the free stream velocity time-series for Case AS (black dash-line), Case VS (solid blue line), and Case AS-VS (red solid line).

transport via velocity skewness. The combination of the flow skewness and asymmetry results in a significant difference between the near-bed load transport rate during the onshore and offshore half-cycles (see the red solid line in 10c) causing a large onshore directed net near-bed load transport rate $< Q_b>_{\rm tx}=19.40\times 10^{-6}m^2/s$. On the other hand, the difference in the suspended load transport rate between the two flow half-cycles (see the blue dash-line in 10c) is reduced compared to the skewed flow. The net suspended load transport rate $< Q_s>_{\rm tx}=-0.8\times 10^{-6}m^2/s$ is offshore directed but much reduced compared to the skewed flow, due to the competition of the positive phase-lag effect (induced by the flow asymmetry) and the negative phase-lag effect (due to the flow skewness).

In summary, model results show that the net total transport rate over the ripple is the largest and onshore-directed under the asymmetric flow as both suspended load and near-bed load transport rates are onshore-directed. In the VS case studied here, velocity skewness causes a large net offshore-directed suspended transport rate due to the negative phase-lag effect, which is larger than the onshore-directed net near-bed load transport rate, and an offshore-directed net total transport rate is obtained. Driven by the asymmetric-skewed flow (case AS-VS), the offshore-directed net suspended load transport rate is reduced compared to the velocity skewed flow due to the contrary phase-lag effects. Importantly, the onshore-directed net near-bed load transport rate is even larger than that under the asymmetric flow due to additional

onshore velocity skewness.

3.4. Near-bed load and ripple migration

Salimi-Tarazouj et al. (2021a) showed the importance of the near-bed load transport rate for migrating ripples. To better illustrate the near-bed load transport differences between these three cases, Fig. 11 is designed to show the time series (horizontal axes) of the dimensionless near-bed load transport rate (ψ_b) along the ripple profile (vertical axes). Under the asymmetric flow (Fig. 11a), a significant onshore directed near-bed load transport is driven over the ripple flanks and crest during the onshore acceleration phase; the maximum near-bed load is occurring around the ripple crest and during the onshore peak velocity

(t/T = 0.2). This is due to erosion of sediments in the boundary layer due to the flow speed up on the ripple flank. When the free-stream velocity starts to decelerate (t/T = 0.22 - 0.4), a negative near-bed load transport pattern forms over the lee flank due to the vortex-induced returning flow ($x/\lambda = 1.6 \sim 1.8$) which is then limited by the onshoredirected sediment avalanching over the lee flank. During the onoffshore flow reversal (t/T = 0.5), the near-bed load transport over the stoss flank is reduced to zero while it is offshore directed in the boundary layer of the lee flank, during the offshore acceleration phase (t/T = 0.5 - 0.7). When the flow reaches its offshore peak and during the deceleration phase (t/T = 0.75 - 9.5), a positive near-bed load transport over the stoss flank is generated by the returning flow of stoss vortex while the sediment avalanching on the stoss flank is not significant. Similar near-bed load transport rate pattern is observed under the skewed (Fig. 11b) and combined flows (Fig. 11c), but with some differences in the transport magnitude. Under the skewed flow, the offshore directed near-bed load transport due to the lee vortex-induced returning flow (t/T = 0.22 - 0.4) is greater compared to that in asymmetric flow (due to stronger lee vortex compared to the asymmetric flow); the onshore near-bed load transport associated with the sediment avalanching is consequently enhanced (t/T=0.25-0.4). Furthermore, during the offshore acceleration phase (t/T = 0.45 - 0.6), the offshore directed near-bed load transport in the boundary layer of the lee flank is larger compared to the asymmetric flow; however, the near-bed load transport associated with the stoss vortex returning flow (during the offshore deceleration phase; t/T = 0.75 - 95) is much lower due to the smaller velocity during the offshore cycle compared to the asymmetric flow. The near-bed load transport during the offshore flow half-cycle (t/ T = 0.48 - 1) is reduced significantly in the combined flow (see Fig. 11c) while a similar near-bed load transport structure as the skewed flow is produced during the onshore flow half-cycle (t/T = 0 - 0.48).

The time series of the ripple-averaged dimensionless near-bed load transport is presented in Fig. 12 (bottom panel) along with the normalized free-stream velocities (top panel) for all three cases. During the onshore acceleration phase (between t/T=0-0.2), the onshore directed near-bed load transport is almost always the largest under the combined flow (red solid line); the skewed (blue solid line) and asymmetric flows (black dash-line) drive smaller near-bed load transport during this phase. Between t/T = 0 - 0.1, the near-bed load transport rates under the skewed and asymmetric flows are nearly the same, however, it is larger under the asymmetric flow between t/T=0.1 – 0.2, due to the smaller offshore directed near-bed load transport associated with the lee vortex-induced returning flow (compare Fig. 11a and b). In other words, the offshore returning flux due to strong lee vortex generation under the skewed flow limits the onshore near-bed load transport rate. During the onshore deceleration phase (t/T = 0.2 - 0.4), the ripple-averaged near-bed load transport under the skewed flow becomes the largest due to the large onshore sediment avalanching occurring under the lee vortex. Although the onshore sediment avalanching under the combined flow is comparable to that of the skewed flow, the large returning flow associated with the lee vortex generation limits the onshore transport rate under the combined flow during this time interval. Hence, during the onshore deceleration phase, the near-bed load transport rate is larger even under the asymmetric flow compared to that under the combined flow. During the offshore acceleration phase (t/T = 0.4 - 0.6), the offshore directed near-bed load transport under the skewed flow is significantly larger than in two other cases due to greater free-stream velocities under the skewed flow during this flow phase. The near-bed load transport rate is larger under the combined flow compared to the asymmetric flow, accordingly. Due to the same reason, during t/T = 0.65 - 0.95, the offshore directed near-bed load transport rate is the largest under the asymmetric flow while it is almost the same for the combined and skewed cases. Slightly before the off-onshore reversal, the onshore directed near-bed load transport in asymmetric flow is larger than the two other cases, due to the stronger stoss vortex generation (positive phase lag effect).

To illustrate ripple migration, Fig. 13a–c presents the ripple profiles for the middle ripple at the selected wave cycle using the contour of volumetric concentration $\varphi=0.57$ for the modeled cases. It is evident that from the start of the simulation, the ripple adjusts its shape and reduces its height, and more importantly migrates slowly to the onshore direction driven by different flow shapes. By tracking the ripple crest based on the ripple profile for each wave cycle, the resulting onshore ripple migration rate is calculated (Fig. 13d). After the first ten wave periods, the migration rate for the asymmetric flow reaches an equilibrium value of $V=24 \, mm/min$ (red symbols in 13d), which is very

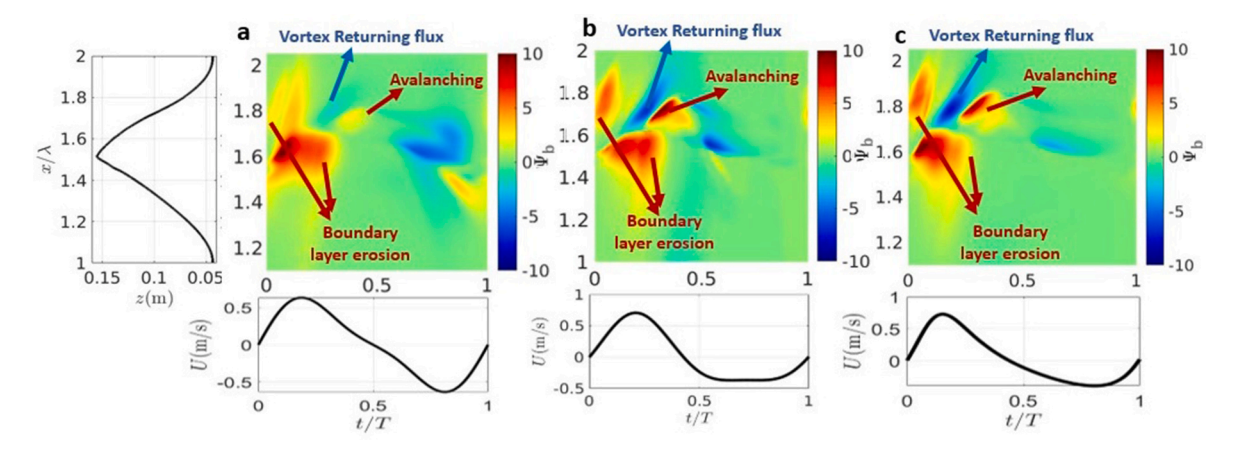


Fig. 11. Time-series of the dimensionless near-bed load (see color-bar) along the ripple profile for Case AS (a), Case VS (b), and Case AS-VS (c) during the last simulation period after the simulations had reach the quasi-equilibrium state. The left panel in each figure shows the ripple profile, for case VS, defined as the contour of volumetric concentration $\varphi=0.57$. The bottom panel in each figure shows the free-stream velocity time series.

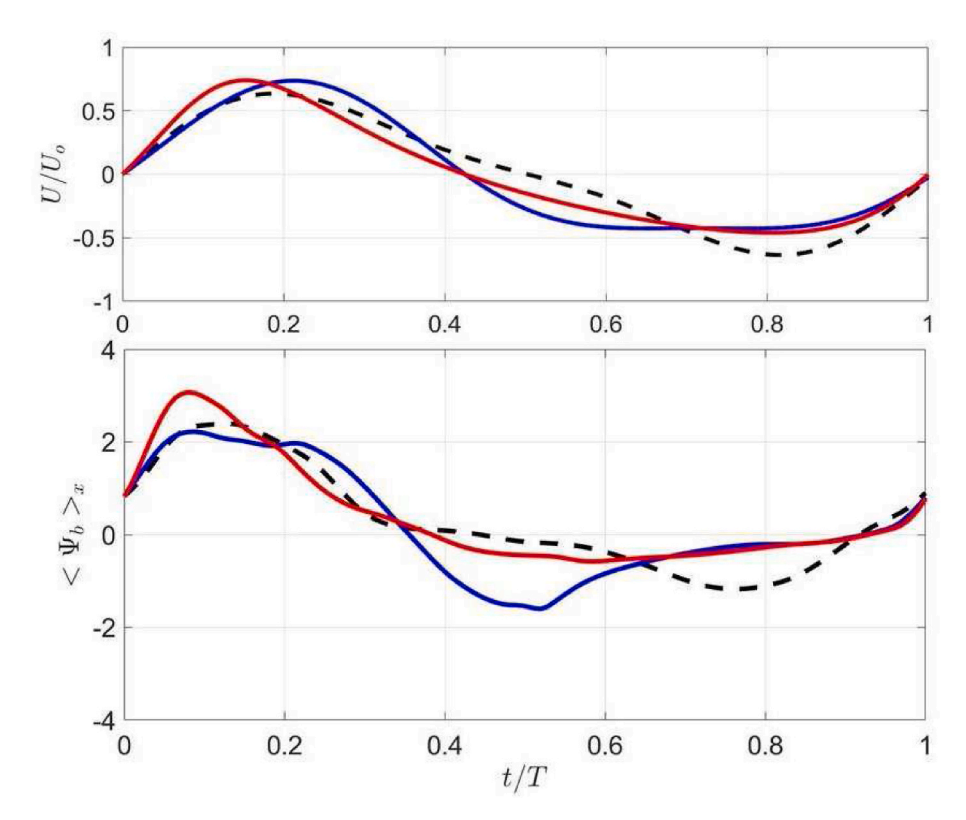


Fig. 12. Time series of ripple-averaged near-bed load transport for Case AS (black dash-line), Case VS (blue solid line), and Case AS-VS (red solid line). The top panel shows the normalized free stream velocity time-series for Case AS (black dash-line), Case VS (solid blue line), and Case AS-VS (red solid line).

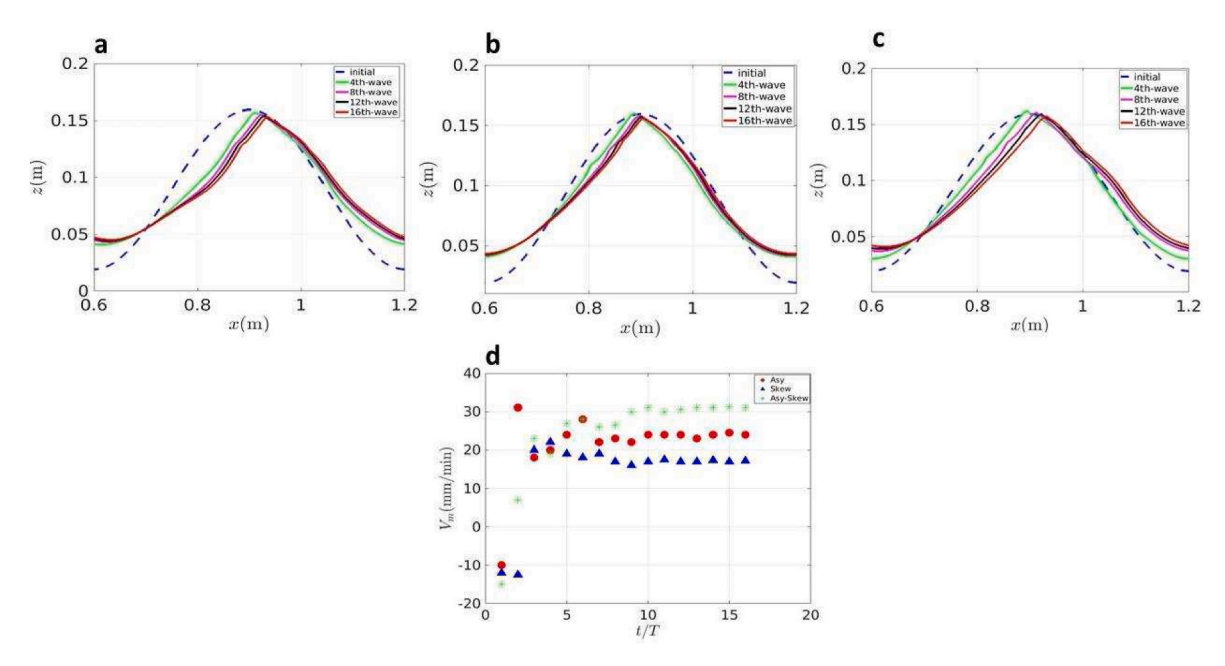


Fig. 13. Ripple profile for the middle ripple in Case AS (a), Case VS (b), and Case AS-VS (c) at different wave cycles visualized using the contour of volumetric concentration $\varphi=0.57$. Panel (d) shows the calculated migration rate for Case AS (red symbols), Case VS (blue symbols), and Case AS-VS (green symbols).

close to the observed migration rate of 22 mm/min reported by Yuan and Wang (2019). The onshore ripple migration rate of V=17 mm/ min forced by the skewed flow is smaller than the ripple migration driven by the asymmetric flow. Meanwhile, driven by the combined flow, the modeled migration rate of V=31 mm/min is the largest. According to the model results, migration rate is directly related to near-bed load transport rate (see Table 2). Although the total net transport rate can be

onshore or offshore directed, the near-bed load transport rates are all onshore directed and consequently, the migration rates are also onshore directed. This is consistent with the van der Werf et al. (2007) experiment.

In summary, the near-bed load transport rate consists of erosion of sediment in the boundary layer due to the flow speed up on the ripple flank, sediment transport due to the vortex-induced returning flow, and sediment avalanching. Due to the large bed shear stress skewness under the combined flow, the near-bed load transport rate difference between the onshore and offshore flow half-cycle is significant. However, under the skewed and asymmetric flows, the onshore near-bed load transport rate under the skewed flow is limited by the offshore directed near-bed load transport due to the strong lee vortex-induced returning flow. On the other hand, the flow asymmetry causes a stronger stoss vortex generation which produces a larger onshore directed near-bed load transport through the stoss vortex-induced returning flow. This contrary vortex generation process leads to a larger net near-bed load transport rate under the asymmetric flow compared to that driven by the skewed flow.

4. Discussion

The results provided in this study correspond to the high energy flow conditions in which the suspended sediment flux is an important sediment transport mechanism. The same analysis should be conducted for ripples driven by low energy flows with different shapes. For instance, for the ripples formed under lower energy flows, the vortex generation-ejection is not intense and the near-bed load fluxes are dominant. Salimi-Tarazouj et al. (2021a, b) showed that the suspended/near-bed load ratio is changing during the transition between different ripple regimes. Hence, the wave-shape effect on sediment transport fluxes may be different for these conditions.

For the present study the coarse sediment $D_{50}=0.51mm$ is utilized. However, it is important to study the wave shape effect on finer sand ripples where the near-bed suspended load ratio will be different. In this study, the near-bed load is calculated using the sediment flux from the bottom of the domain to the vertical location z_{50} which is $20\,D_{50}$ above the ripple's surface (following the ripple shape). This location is chosen to include the all the near-bed load transport mechanisms (boundary layer erosion, sediment avalanching, and the vortex induced returning flux). However, for the finer sand, this vertical location might be different.

The RANS model used in this study, although computationally efficient, may struggle to capture fine-scale turbulent behaviors near the bed, leading to less accurate modeling of sediment transport over migrating ripples, Hence, it is important to employ Large Eddy Simulation (LES) turbulence model for providing a detailed and high-resolution representation of turbulent flows, enabling the accurate simulation of complex interactions between sediment-laden flows and ripple bedforms. By resolving smaller-scale turbulence structures, LES enhances the ability to predict sediment transport, bedform evolution, and boundary layer dynamics with precision, making it an invaluable tool for studying the formation, migration, and morphological changes of the sand ripples.

Yuan and Wang (2019) reported the presence of the small humps in the trough locations of the ripples driven by the asymmetric oscillatory flows; however, the humps are absent in the modeled ripples. Salimi-Tarazouj et al. (2021b) also showed the formation of these small humps in the trough location for the ripple formation from a near flatbed. The mechanism behind the formation of these humps and their effect on the flow and sediment transport fluxes are not explained by Yuan and Wang (2019). Hence, a more detailed investigation is necessary to understand the formation of these secondary bathymetric features in the larger ripple's trough location.

5. Conclusion

In this study, an Eulerian two-phase model for sediment transport, SedFoam has been utilized to investigate the effect of wave shape on the sediment transport over migrating ripples. By keeping the same sediment grain size, flow period, and mobility number, three ripple simulations driven by skewed and/or asymmetric oscillatory flows are conducted. The asymmetric case is similar to the oscillating tunnel

experiments conducted by Yuan and Wang (2019), which also serve the purpose of model validation. The model results show a very good agreement with measured data for ripple dimensions, velocity field, net sediment transport, and ripple migration rates.

Model results confirmed that under the asymmetric flow, the stoss vortex generation-ejection process is expedited by higher onshore acceleration which causes a more energetic stoss vortex, compared to the lee vortex. As a result, the stoss vortex can travel further toward the onshore direction as it is carried by the faster onshore ambient flow. Faster and stronger stoss vortex generation-ejection causes an onshore directed net suspended load transport rate through the positive phaselag effect. In contrast, driven by the skewed flow, the negative phaselag effect due to the strong lee vortex generation-ejection process drives offshore directed net suspended load transport rate. These contradicting phase-lag effects, co-existing under the combined flow, reduce the net offshore directed suspended load transport rate. Model results reveal that the near-bed load sediment transport is due to the sediment erosion in the accelerating boundary layer over each ripple flank, sediment flux due to vortex-induced returning flow which is limited by the sediment avalanching. The net near-bed load transport rates which force the ripple migration are onshore directed for all three cases. The nearbed load transport rate (and ripple migration) is largest under the combined oscillatory flow due to a large onshore shear skewness. Although the skewness values are fairly the same for the skewed and asymmetric cases, the net onshore directed near-bed load transport rate driven by the asymmetric flow is greater than that driven by the skewed flow. The offshore directed near-bed load flux due to the lee vortexinduced returning flow limits the net onshore directed near-bed load transport rate under the skewed flow while the returning flow under the stoss vortex increases the net onshore directed near-bed load under the asymmetric flow. Consequently, the ripple migration rate is larger under the asymmetric flow compared to the skewed flow. Finally, model results indicate that the net sediment transport rate is largest and onshore directed under the asymmetric flow as both the suspended load and near-bed load transport rates are onshore directed. The larger offshore directed suspended load compared to the onshore directed near-bed load transport rate causes an offshore directed net transport rate under the skewed flow. Compared to the asymmetric flow, the net onshore directed transport rate driven by the combined flow is slightly reduced, due to the small net offshore directed suspended transport rate.

CRediT authorship contribution statement

Ali Salimi-Tarazouj: Conceptualization, Data curation, Formal analysis, Investigation, Methodology, Software, Validation, Visualization, Writing – original draft, Writing – review & editing. Tian-Jian Hsu: Funding acquisition, Methodology, Project administration, Supervision. Peter Traykovski: Methodology, Writing – review & editing. Julien Chauchat: Methodology, Writing – review & editing.

Declaration of competing interest

The authors declare that they have no known competing financial interests or personal relationships that could have appeared to influence the work reported in this paper.

Data availability

Data will be made available on request.

Acknowledgements

This study is supported by National Science Foundation (OCE-1635151 and OCE-2242113) and Office of Naval Research (N00014-221-2412). Numerical simulations presented in this study were carried out using the Caviness cluster at University of Delaware, We are grateful to

the developers involved in OpenFOAM, who are the foundation of the model presented in this paper. The source code is publicly available via the SedFOAM's official website: http://servforge.legi.grenoble-inp.fr/

pub/soft-sedfoam/or GitHub repository: https://github.com/Ali-Salim i/sedfoam (source code).

Appendix A

This section offers a concise overview of the governing equations. For a more comprehensive understanding, Salimi-Tarazouj et al. (2021a) contains detailed information on this topic.

In SedFoam, both fluid and sediment phases are modeled as a continuum using their incompressible mass conservation equations:

$$\frac{\partial(1-\varphi)}{\partial t} + \frac{\partial(1-\varphi)u_i^f}{\partial x_i} = 0 \tag{A.1}$$

$$\frac{\partial \varphi}{\partial t} + \frac{\partial \varphi u_i^s}{\partial x_i} = 0 \tag{A.2}$$

and momentum conservation equation:

$$\frac{\partial \rho^f (1 - \varphi) u_i^f}{\partial t} + \frac{\partial \rho^f (1 - \varphi) u_i^f u_j^f}{\partial x_j} = -(1 - \varphi) \frac{\partial P^f}{\partial x_i} + (1 - \varphi) f_i + \frac{\partial \tau_{ij}^f}{\partial x_j} - \rho^f (1 - \varphi) g \delta_{i2} + M_i^{fs}$$
(A.3)

$$\frac{\partial \rho^s \varphi u_i^s}{\partial t} + \frac{\partial \rho^s \varphi u_i^s u_j^s}{\partial x_j} = -\varphi \frac{\partial P^f}{\partial x_i} + \varphi f_i - \frac{\partial P^s}{\partial x_i} + \frac{\partial \tau_{ij}^s}{\partial x_j} - \rho^s \varphi g \delta_{i2} + M_i^{sf}$$
(A.4)

where u_i^f and u_i^s represents fluid and sediment phase velocities, respectively, and tensor notation with the subscript i (or j) = 1, 2 is used to represent streamwise (x) and vertical (z) directions. Sediment volumetric concentration is expressed by φ . In equations A.3 and A.4, P^f is the fluid pressure, $\rho^f = 1000 \ (kg/m^3)$ and $\rho^s = 2650 \ (kg/m^3)$ are water and sand grain density, respectively, and $g = 9.81 \ (m/s^2)$ is the gravitational acceleration. f_i is the external force that drives the flow. The fluid stress τ^f_{ij} includes fluid grain-scale (viscous) stress and fluid Reynolds stresses, P^s , and τ^s_{ij} are particle normal stress and shear stress. The last term on the right-hand side (RHS) of equations (3) and (4) is momentum coupling between the fluid phase and particle phase through drag force $[M_i^{g}] = M_i^{gf}$ (see Salimi-Tarazouj et al., 2021a for more detail).

The particle phase stress tensor can be split into the normal and off-diagonal components corresponding to the particle pressure P^s and the particle shear stress τ^s_{ij} , respectively. Particle phase pressure and shear stress are modeled by a collisional component (super-script 'sc') in the low to intermediate concentration regime, and a frictional component (super-script 'sf') for high concentration regime of enduring contact,

$$P^{s} = P^{sc} + P^{sf} \tag{A.5}$$

$$\tau_{ii}^s = \tau_{ii}^{sc} + \tau_{ii}^{sf} \tag{A.6}$$

We adopt the kinetic theory of granular flow for the collisional components (P^{sc} , τ_{ij}^{sc}) based on the granular temperature (defined as one-third of the kinetic energy of particle velocity fluctuation) (See Cheng et al., 2017; Salimi-Tarazouj et al., 2021a for more detail). The particle pressure due to elastic/frictional contact in the highly concentrated region is calculated following Johnson et al. (1990) to model the elastic behavior of the sediment hed:

$$P^{\text{sf}} = \begin{cases} 0, \varphi_c < 0.57 \\ 0.05 \frac{(\varphi - 0.57)^3}{(0.635 - \varphi)^5}, \varphi_c \ge 0.57 \end{cases}$$
(A.7)

The particle shear stress in the highly concentrated quasi-static (nearly zero shear rate) region is modeled as,

$$\tau_{ij}^{g} = 2\rho^{s} \nu_{F_{r}} S_{ij}^{s} \tag{A.8}$$

where ν_{Fr}^s is the frictional viscosity and S_{ij}^s is the deviatoric part of the sediment phase strain rate. A friction viscosity is readily calculated by relating the particle pressure and particle shear stress by a frictional angle θ_f (Schaeffer, 1987),

$$\nu_{Fr}^{s} = \frac{P^{sf} \sin\left(\theta_{f}\right)}{\rho^{s} \left(\left|S_{ij}^{s}\right|^{2} + D_{small}^{2}\right)^{1/2}} . \tag{A.9}$$

As outlined by Salimi-Tarazouj et al. (2021a), θ_f governs the threshold angle for the resolved avalanching process during ripple migration and is set to $\theta_f = 32^o$ in line with the angle of repose for cohesionless sand grains. To ensure numerical stability, especially when the shear rate approaches zero in highly sediment-concentrated regions near the immobile bed, a regularization technique (Chauchat and Médale, 2014) is employed with $D_{small} = 10e - 10$ specified.

In all cases presented within this study, sediment phase stress closures, along with their corresponding coefficients and parameters, remain consistent with those employed in Salimi-Tarazouj et al. (2021a and b). For a comprehensive understanding of the k- ϵ turbulence closure model and the collisional and frictional components of particle stress, detailed expressions can be found in Salimi-Tarazouj et al. (2021a).

References

- Abreu, T., Silva, P.A., Sancho, F., Temperville, A., 2010. Analytical approximate wave form for asymmetric waves. Coast. Eng. 57 (7), 656–667. https://doi.org/10.1016/j. coastaleng.2010.02.005.
- Bagnold, R.A., 1966. An Approach to the Sediment Transport Problem from General Physics. U.S. Government Printing Office, United States.
- Blondeaux, P., Vittori, G., 1991. Vorticity dynamics in an oscillatory flow over a rippled bed. J. Fluid Mech. 226 (WW1), 257–289. https://doi.org/10.1017/
- Chang, Y.S., Hanes, D.M., 2004. Suspended sediment and hydrodynamics above mildly sloped long wave ripples. J. Geophys. Res.: Oceans 109 (C7). https://doi.org/ 10.1029/2003/C001900.
- Chauchat, J., Médale, M., 2014. A three-dimensional numerical model for dense granular flows based on the μ(I) rheology. J. Comput. Phys. 256, 696–712. https://doi.org/ 10.1016/j.jcp.2013.09.004.
- Chauchat, J., Cheng, Z., Nagel, T., Bonamy, C., Hsu, T.-J., 2017. SedFoam-2.0: a 3-D Two-phase Flow Numerical Model for Sediment Transport, pp. 4367–4392. https://doi.org/10.5194/gmd-10-4367-2017, 105194.
- Cheng, Z., Hsu, T.J., Calantoni, J., 2017. SedFoam: a multi-dimensional Eulerian two-phase model for sediment transport and its application to momentary bed failure. Coast. Eng. 119, 32–50. https://doi.org/10.1016/j.coastaleng.2016.08.007.
- Chou, Y.J., Fringer, O.B., 2010. A model for the simulation of coupled flow-bed form evolution in turbulent flows. J. Geophys. Res.: Oceans 115 (10), 1–20. https://doi. org/10.1029/2010.IC006103.
- Dibajnia, M., Watanabe, A., 1998. Transport rate under irregular sheet flow conditions. Coast. Eng. 35 (3), 167–183. https://doi.org/10.1016/S0378-3839(98)00034-9.
- Dohmen-Janssen, C.M., Hanes, D.M., 2002. Sheet flow dynamics under monochromatic nonbreaking waves. J. Geophys. Res. 107 (C10), 1–21. https://doi.org/10.1029/ 2001JC001045.
- Dong, L.P., Sato, S., Liu, H., 2013. A sheetflow sediment transport model for skewed-asymmetric waves combined with strong opposite currents. Coast. Eng. 71, 87–101. https://doi.org/10.1016/j.coastaleng.2012.08.004.
- Finn, J.R., Li, M., Apte, S.V., 2016. Particle based modelling and simulation of natural sand dynamics in the wave bottom boundary layer. J. Fluid Mech. 796, 340–385. https://doi.org/10.1017/jfm.2016.246.
- Hurther, D., Thorne, P.D., 2011. Suspension and near-bed load sediment transport processes above a migrating, sand-rippled bed under shoaling waves. J. Geophys. Res.: Oceans 116 (7), 1–17. https://doi.org/10.1029/2010JC006774.
- Johnson, P.C., Nott, P., Jackson, R., 1990. Frictional-collisional equations of motion for participate flows and their application to chutes. J. Fluid Mech. 210, 501–535, 10.1017/S0022112090001380.
- King Jr., D.B., 1991. Studies in oscillatory flow bedload sediment transport (Order No. 9130729). In: Available from ProQuest Dissertations & Theses Global, 303950342. Retrieved from. https://www.proquest.com/dissertations-theses/studies-oscillatory-flow-bedload-sediment/docview/303950342/se-27accountid=10457.
- Kranenburg, W.M., Ribberink, J.S., Schretlen, J.J.L.M., Uittenbogaard, R.E., 2013. Sand transport beneath waves: the role of progressive wave streaming and other free surface effects. J. Geophys. Res. Earth Surf. 118, 122–139. https://doi.org/10.1029/ 2012JF002427.
- Lanckriet, T., Puleo, J.A., 2015. A semianalytical model for sheet flow layer thickness with application to the swash zone. J. Geophys. Res. Oceans 120, 1333–1352. https://doi.org/10.1002/2014JC010378.
- Longuet-Higgins, M.S., 1953. Mass transport in water waves. Philos. Trans. R. Soc. London, Ser. A 245 (903), 535–581.
- Longuet-Higgins, M., 1981. Oscillating flow over steep sand ripples. J. Fluid Mech. 107, 1–35. https://doi.org/10.1017/S0022112081001651.
- Marieu, V., Bonneton, P., Foster, D.L., Ardhuin, F., 2008. Modeling of vortex ripple morphodynamics. J. Geophys. Res.: Oceans 113 (9), 1–15. https://doi.org/10.1029/ 2007JC004659.
- Nielsen, P., 1981. Dynamics and geometry of wave-generated ripples. J. Geophys. Res. 86 (C7), 6467–6472. https://doi.org/10.1029/JC086iC07p06467.
- Önder, A., Yuan, J., 2019. Turbulent dynamics of sinusoidal oscillatory flow over a wavy bottom. J. Fluid Mech. 858, 264–314. https://doi.org/10.1017/jfm.2018.754.
- Rafati, Y., Hsu, T.-J., Elgar, S., Raubenheimer, B., Quataert, E., van Dongeren, A., 2021.
 Modeling the hydrodynamics and morphodynamics of sandbar migration events.
 Coast. Eng. 166, 103885 https://doi.org/10.1016/j.coastaleng.2021.103885.

- Ribberink, J.S., van der Werf, J.J., O'Donoghue, T., Hassan, W.N.M., 2008. Sand motion induced by oscillatory flows: sheet flow and vortex ripples. J. Turbul. 9, 1–32. https://doi.org/10.1080/14685240802220009.
- Ruessink, B.G., Michallet, H., Abreu, T., Sancho, F., Van Der A, D.A., Van Der Werf, J.J., Silva, P.A., 2011. Observations of velocities, sand concentrations, and fluxes under velocity-asymmetric oscillatory flows. J. Geophys. Res.: Oceans 116 (3), 1–13. https://doi.org/10.1029/2010JC006443.
- Salimi-Tarazouj, A., Hsu, T.J., Traykovski, P., Cheng, Z., Chauchat, J., 2021a.
 A numerical study of onshore ripple migration using a eulerian two-phase model.
 J. Geophys. Res.: Oceans 126 (2), 1–27. https://doi.org/10.1029/2020JC016773.
- Salimi-Tarazouj, A., Hsu, T., Traykovski, P., Chauchat, J., 2021b. Eulerian two-phase model reveals the importance of wave period in ripple evolution and equilibrium geometry. J. Geophys. Res.: Earth Surf. 126 (7), 1–28. https://doi.org/10.1029/ 2021f006132
- Schaeffer, D.G., 1987. Instability in the evolution equations describing incompressible granular flow. J. Differ. Equ. 66 (1), 19–50. https://doi.org/10.1016/0022-0396(87) 90038-6.
- Scherer, M., Uhlmann, M., Kidanemariam, A.G., Krayer, M., 2022. On the role of turbulent large-scale streaks in generating sediment ridges. J. Fluid Mech. 930, A11. https://doi.org/10.1017/jfm.2021.891.
- Schretlen, J.L.M., 2012. Sand Transport under Full-Scale Progressive Surfacewaves, PhD Thesis. University of Twente, Enschede, Netherlands [Available at: http://doc.utwepten/80884
- Sherwood, C.R., van Dongeren, A., Doyle, J., Hegermiller, C.A., Hsu, T.-J., Kalra, T.S., et al., 2022. Modeling the morphodynamics of coastal responses to extreme events: what shape are we in? Ann. Rev. Mar. Sci 14 (1), 457–492. https://doi.org/10.1146/annurev-marine-032221-090215.
- Thornton, E.B., Swayne, J.L., Dingler, J.R., 1998. Small-scale morphology across the surf zone. Mar. Geol. 145 (3–4), 173–192. https://doi.org/10.1016/S0025-3227(97) 00114-X.
- Traykovski, P., Hay, A.E., Irish, J.D., Lynch, J.F., 1999. Geometry, migration, and evolution of wave orbital ripples at LEO-15. J. Geophys. Res.: Oceans 104 (C1), 1505–1524. https://doi.org/10.1029/1998JC900026.
- van der Werf, Jabbe, J., Doucette, J.S., O'Donoghue, T., Ribberink, J.S., 2007. Detailed measurements of velocities and suspended sand concentrations over full-scale ripples in regular oscillatory flow. J. Geophys. Res.: Earth Surf. 112 (F2).
- van der Werf, J.J., Magar, V., Malarkey, J., Guizien, K., O'Donoghue, T., 2008. 2DV modelling of sediment transport processes over full-scale ripples in regular asymmetric oscillatory flow. Continental Shelf Research. https://doi.org/10.1016/j.csr.2008.02.007.
- vander, A., Ribberink, Jan S., Jebbe, J., vander, Werf, O'Donoghue, Tom, Buijsrogge, René H., Kranenburg, Wouter M., 2013. Practical sand transport formula for non-breaking waves and currents. Coast. Eng. 76, 26–42. https://doi.org/ 10.1016/i.coastaleng.2013.01.007. ISSN 0378-3839.
- Wang, D., Yuan, J., 2019. Geometric characteristics of coarse-sand ripples generated by oscillatory flows: a full-scale experimental study. Coast. Eng. 147 (December 2018), 159–174. https://doi.org/10.1016/j.coastaleng.2019.02.007.
- Wang, D., Yuan, J., 2020. Modeling of net sediment transport rate due to wave-driven oscillatory flow over vortex ripples. Appl. Ocean Res. 94, 101979 https://doi.org/ 10.1016/j.apor.2019.101979. September 2019.
- Watanabe, A., Sato, S., 2005. A sheet-flow transport rate formulae for asymmetric, forward-leaning waves and currents. Coast. Eng. 2004, 1703–1714. https://doi.org/ 10.1142/9789812701916_0136. World Scientific Publishing Company.
- Wengrove, M.E., Foster, D.L., Lippmann, T.C., de Schipper, M.A., Calantoni, J., 2018. Observations of time-dependent bedform transformation in combined wave-current flows. J. Geophys. Res.: Oceans 123 (10), 7581–7598. https://doi.org/10.1029/ 2018JC014357.
- Wengrove, M.E., Foster, D.L., Lippmann, T.C., de Schipper, M.A., Calantoni, J., 2019. Observations of bedform migration and bedload sediment transport in combined wave-current flows. J. Geophys. Res.: Oceans 124 (7), 4572–4590. https://doi.org/ 10.1029/2018JC014555.
- Yuan, J., Wang, D., 2019. An experimental investigation of acceleration-skewed oscillatory flow over vortex ripples. J. Geophys. Res.: Oceans 124 (12), 9620–9643. https://doi.org/10.1029/2019JC015487.
- Zedler, E.A., Street, R.L., 2006. Sediment transport over ripples in oscillatory flow.
 J. Hydraul. Eng. 132 (2), 180–193. https://doi.org/10.1061/(asce)0733-9429, 2006)132:2(180.